preprint from CCP Summary Volume 2 (Elsevier, fall 2004)

Reactive transport modeling of cap rock integrity during natural and engineered CO_2 storage

Chapter Authors

- James W. Johnson, Research Scientist, Environmental Sciences Div., LLNL
- John J. Nitao, Research Scientist, Environmental Sciences Div., LLNL
- Joseph P. Morris, Research Scientist, Earth Sciences Div., LLNL

Abstract

Long-term cap rock integrity represents the single most important constraint on the long-term isolation performance of natural and engineered CO_2 storage sites. CO_2 influx that forms natural accumulations and CO_2 injection for EOR/sequestration or saline-aquifer disposal both lead to concomitant geochemical alteration and geomechanical deformation of the cap rock, enhancing or degrading its seal integrity depending on the relative effectiveness of these interdependent processes. Using our reactive transport simulator (NUFT), supporting geochemical databases and software (GEMBOCHS, SUPCRT92), and distinct-element geomechanical model (LDEC), we have shown that influx-triggered mineral dissolution/precipitation reactions within typical shale cap rocks continuously reduce microfracture apertures, while pressure and effective-stress evolution first rapidly increase then slowly constrict them. For a given shale composition, the extent of geochemical enhancement is nearly independent of key reservoir properties (permeability and lateral continuity) that distinguish EOR/sequestration and saline-aquifer settings and CO_2 influx parameters (rate, focality, and duration) that distinguish engineered disposal sites and natural accumulations, because these characteristics and parameters have negligible (indirect) impact on mineral dissolution/precipitation rates. In contrast, the extent of geomechanical degradation is highly dependent on these reservoir properties and influx

parameters because they effectively dictate magnitude of the pressure perturbation. Specifically, initial geomechanical degradation has been shown inversely proportional to reservoir permeability and lateral continuity and proportional to influx rate. Hence, while the extent of geochemical alteration is nearly independent of filling mode, that of geomechanical deformation is significantly more pronounced during engineered storage. This suggests that the currently secure cap rock of a given natural CO_2 accumulation may be incapable of providing an effective seal in the context of an engineered injection, a potential discrepancy that limits the extent to which natural CO_2 reservoirs and engineered storage sites can be considered analogous. In addition, the pressure increase associated with CO_2 accumulation in any compartmentalized system invariably results in net geomechanical aperture widening of cap-rock microfractures. This suggests that ultimate restoration of pre-influx hydrodynamic seal integrity—in both EOR/sequestration and natural accumulation settings—hinges on ultimate geochemcial counterbalancing of this geomechanical effect. To explore this hypothesis, we have introduced a new conceptual framework that depicts such counterbalancing as a function of effective diffusion distance and reaction progress. This framework reveals that ultimate counterbalancing of geochemical and geomechanical effects is feasible, which suggests that shale cap rocks may in fact *evolve* into effective seals in both natural and engineered storage sites.

Introduction

Sufficient curbing of projected anthropogenic CO_2 emissions to achieve a stabilized “safe” atmospheric concentration ranks high among the grand challenges of this century. In the near term, significant emissions reduction can only be achieved through innovative capture/isolation strategies applied to point-source waste streams. Among currently proposed isolation techniques, injection into confined geologic formations represents one of the most promising alternatives. Oil reservoirs, where CO_2 storage and EOR can be co-optimized, and saline aquifers, which feature immense storage capacity and widespread geographic distribution, represent particularly attractive geologic targets.

Successful engineered CO_2 storage in these environments hinges on our ability to identify optimal sites and forecast their long-term security. This ability, in turn, relies upon predictive models for assessing the relative effectiveness of CO_2 migration and sequestration processes (isolation performance) as a function of key target-formation and cap-rock properties (screening criteria). It also relies on detailed knowledge of naturally-occuring CO_2 reservoirs and clear understanding of the extent to which they represent natural analogs to engineered storage sites. Among key screening criteria, long-term cap rock integrity represents the single most important constraint on the long-term isolation performance of both natural and engineered CO_2 storage sites. And among predictive methodologies, the reactive transport modeling approach is uniquely well-suited to quantify this fundamental constraint.

In this study, we have extended and applied our computational toolbox to address this central issue of long-term hydrodynamic seal capacity. In the development phase, we first interfaced our existing reactive transport and geomechanical modeling capabilities to facilitate assessment of stress-strain evolution along and above the reservoir/cap-rock contact during and after CO_2 influx. We then constructed a new conceptual framework for evaluating the net impact on long-term cap rock integrity of influx-triggered geochemical alteration and geomechanical deformation processes.

In the application phase, we have used our modeling capabilities to address two fundamental questions. First, what is the evolution of cap-rock integrity during engineered CO_2 storage—and does this evolution vary significantly between EOR/sequestration and saline aquifer settings? This work builds directly upon our earlier modeling studies, which demonstrated enhanced hydrodynamic seal capacity of shale cap rocks as a function of injection-triggered geochemical processes during saline aquifer disposal [**1-4**]. Here, these earlier analyses have been extended to include explicit account of the concomitant geomechanical processes, and to assess

dependence of this coupled geochemical-geomechanical evolution on key reservoir properties (permeability and lateral continuity) that distinguish typical oil reservoirs and saline aquifers [**5-6**].

We then address a closely related key issue: is the predicted evolution of cap-rock integrity for engineered CO_2 disposal sites similar to or appreciably different from that of natural CO_2 accumulations; i.e., what is the dependence of this evolution on the rate, duration, and focality of CO_2 influx? The widely espoused natural analog concept implicitly assumes a dearth of such dependence; however, this assumption—upon which strict validity of the concept hinges—may be invalid in some cases. For example, a given reservoir/cap rock system that now holds a natural CO_2 accumulation may be incapable of doing so in the context of an engineered injection owing to significant differences in the magnitude and style of CO_2 influx. Further, the currently secure cap rock of a given natural accumulation may have *evolved* into an effective hydrodynamic seal following geochemical alteration that attended some degree of CO_2 migration through it. To address these issues, we have conducted and compared reactive transport simulations of a representative generic natural CO_2 reservoir for natural and engineered "filling" modes [**7-8**].

Because cap-rock integrity represents the ultimate constraint on the long-term isolation performance of geologic CO_2 storage sites, our reactive transport modeling analysis is linked to a number of additional CCP-funded studies presented in this volume [**9-14**]. There are potential direct links to three studies: the SAMCARDS analysis of Wildenborg et al. [**9**], into which our simulation results could be directly incorporated, and the natual analog and experimental studies of Stevens et al. [**10**] and Borm et al. [**11**], respectively, with which future coordinated efforts might provide field- and laboratory-scale "proof of concept" for our modeling capabilities. In addition, the reactive transport modeling approach used here could be employed to simulate the advective and diffusive migration of imposed anomalies in noble gas isotope ratios, as measured in the field by Nimz et al. [**12**]; to generate the fluid-phase pressures, saturations, densities, and viscosites required to predict dependent geophysical properties, as discussed by Hoversten et al.

[**13**]; and to predict the migration paths of CO_2-charged fluids within magma-hydrothermal systems, as inferred from field measurements by Evans et al. [**14**].

Methodology

Reactive transport modeling is an advanced computational method for quantitatively predicting the long-term consequences of natural or engineered perturbations to the subsurface environment [**15-16**]. Because these predictions typically involve space, time, and system complexity scales that preclude development of direct analytical or experimental analogs, they often represent a unique forecasting tool. The necessary point of departure for predictive investigations of this kind is established by successful application of the method to simulate well-constrained laboratory experiments [**17-18**].

The method is based on mathematical models of the integrated thermal, hydrological, geochemical, and geomechanical processes that redistribute mass and energy in response to the disequilibrium state imposed by perturbation events such as magmatic intrusion or CO_2 influx (**Figure 1**). Traditionally, such models have been developed as separate entities and applied as such to address specific issues relevant their individual scope. The fundamental advance embodied in reactive transport modeling is its explicit integration of these conceptually distinct process models. In practice, however, present-day simulators address and couple various subsets of these models, while the ultimate simulation tool—one that implements and explicitly couples all of the relevant processes—remains on the horizon.

We have developed a unique computational capability that integrates a state-of-the-art reactive transport simulator (NUFT), comprehensive supporting geochemical software and databases (SUPCRT92, GEMBOCHS), and a versatile distinct-element geomechanical model (LDEC). NUFT [19-20] is a software package that facilitates numerical simulation of non-isothermal multiphase/multicomponent flow and reactive transport within a wide range of subsurface

environments characterized by multi-scale physical and compositional heterogeneity. The package implements an integrated finite-difference spatial discretization to solve the flow and reactive-transport equations, using the Newton-Raphson method to solve the resulting nonlinear systems at each time step. Explicit account is taken of multiphase advection, diffusion, and dispersion; of relative permeability and capillary pressure, using an extended Van Genuchten formulation [21]; and of kinetically controlled fluid-mineral reactions, using rate laws from transition state theory [22]. Moreover, explicit account is also taken of *coupling between* these transport and geochemical processes through the dependence of permeability on porosity changes due to mineral precipitation/dissolution, using a normalized Kozeny equation [23], and through the dependence of fluid-phase volumetric saturations on gas (e.g., CO_2(g)) generated or consumed by fluid-mineral reactions.

The GEMBOCHS system [**24-25**] integrates a comprehensive relational thermodynamic/kinetic database and dedicated software library that together facilitate generation of application-specific thermodynamic/kinetic datafiles for use with a variety of geochemical modelling codes and reactive transport simulators. The thermodynamic database covers about 3200 distinct chemical species, spanning 86 elements of the periodic table; its core component is the current version of the SUPCRT92 database [**26-27**], which covers about 1550 species, spanning 82 elements. Custom datafiles are generated using Jewel [**24**], a GUI-driven software package that extrapolates reference-state properties to elevated P-T conditions using a number of standard algorithms, the core set of which are those encoded with the SUPCRT92 software package [**26**]. These include global- and critical-region equations of state and a dielectric formulation for H_2O [**28**] that are explicitly integrated with equations of state for both aqueous solutes [**29-30**] and minerals/gases [**31**].

LDEC [**32-33**] is a geomechanical model that implements the distinct element method, which facilitates representation of fractured rock mass using arbitrary polyhedra, detection of new

contacts between blocks resulting from relative block motion using the "Common-Plane" approach [**34**], exact conservation of linear and angular momentum, and simplified tracking of material properties as blocks move. Use of an explicit integration scheme allows extreme flexibility with respect to joint constitutive models, which here include effects such as cohesion, joint dilation, and friction angle. Both rigid and deformable approximations to block response are implemented. The rigid block approximation assumes that the compliance of fractured rock mass is closely approximated by lumping all compliance at the joints alone; however, this formulation also includes an optional second joint stiffness term that approximates deformation of the rock matrix.

The current method for one-way coupling between NUFT and LDEC represents our integrated model's key approximation. Specifically, the NUFT-LDEC interface facilitates mapping pressure evolution into the corresponding effective stress, fracture aperture, and permeability history; however, at present, this geomechanical-dependent evolution (LDEC) is not back-coupled into the multiphase flow and reactive transport model (NUFT). As a result, the dependence of permeability, fluid flow, and pressure (including capillary pressure) evolution on concomitant geomechanical aperture history is not represented. In the present study, the NUFT-LDEC interface is used to translate the CO_2 influx-triggered pressure perturbation within basal cap rock into the corresponding evolution of effective stress and microfracture apertures, which permits first-order assessment of influx-induced geomechanical deformation. It is important to recognize that in the context of a bi-directionally coupled multiphase flow and geomechanical model, the magnitude of this pressure perturbation would likely be diminished—through concomitant evolution (initial widening) of cap-rock microfracure apertures—relative to that predicted here. Owing to their functional dependence on such magnitude, both the extent of CO_2 migration into undeformed cap rock and that of aperture widening predicted by the present one-way coupled model should be viewed as upper-limit values; on the other hand, likely enhanced advective CO_2 migration through initially widened microfractures is not accounted for here.

In order to evaluate the net impact on long-term cap rock integrity of concomitant geochemical and geomechanical processes, we introduce a new conceptual model that depicts geochemical counterbalancing of geomechanical aperture evolution as a function of effective diffusion distance and reaction progress. This model provides a theoretical framework for assessing the extent to which cap-rock integrity will ultimately be enhanced or degraded in specific reservoir/cap-rock systems in the context of specific CO_2 influx scenarios.

Results and Discussion

Predicting long-term permeability evolution within the cap-rock environment of CO_2 storage sites requires first identifying, then quantifying its functional dependence on key system parameters and dynamic processes. The most important factors influencing this evolution are conveniently subdivided into three groups: intrinsic cap rock properties, chemical conditions at the reservoir/cap-rock interface, and the CO_2 influx-triggered pressure perturbation.

Relevant cap-rock properties include geomechanical parameters, such as fracture normal stiffness, and geochemical characteristics, such as bulk concentrations of carbonate-forming cations—principally Fe, Mg, Ca, Na, and Al. These cation concentrations represent the primary control on geochemical alteration processes, while chemical conditions at the reservoir/cap-rock interface, which are determined by reservoir compositions and CO_2 waste-stream impurities (e.g., CH_4, H_2S, SO_x,NO_x concentrations), exert a secondary control. Magnitude, duration, and focality of the injection-induced pressure perturbation—which depend on these same characteristics of CO_2 influx as well as on reservoir permeability, lateral continuity, compartment height (for laterally confined settings), depth, and thickness—represent the fundamental controls on geomechanical deformation processes.

In the context of these dependencies, long-term enhancement or degradation of cap rock integrity

hinges on the relative contributions of geochemical alteration, which tends to reduce microfracture apertures in typical shale, and geomechanical deformation, which widens them (**Figure 2**). As a result, long-term performance forecasting of potential CO_2 storage sites requires a predictive capability that quantifies this pivotal interplay of geochemical and geomechanical processes. Previously, we have modeled the geochemical contribution within a full system analysis of coupled hydrological and geochemical processes [**1-4**]. Here, we first assess the geomechanical contribution—through analysis of its dependence on hydrological processes, key reservoir properties, and CO_2 influx parameters—then evaluate the ultimate net effect of opposing geochemical and geomechanical contributions to cap-rock integrity for both natural and engineered storage scenarios.

In describing this work, we begin with a review of subsurface CO_2 migration and sequestration processes, which provides not only the geochemical contribution to long-term cap rock integrity, but also full-system context for the subsequent analysis, which focuses on the cap rock environment.

Subsurface CO_2 migration and sequestration processes

Our previous modeling studies [**1-4**] have been largely based on simulating CO_2 injection at Statoil's North-Sea Sleipner facility—the world's first commercial saline-aquifer storage site. Here, CO_2-rich natural gas is produced from 3500 m below the seabed. Excess CO_2 is removed by amine absorption on the platform, then stripped from the amine, and finally injected—at the rate of one million tons per year since 1996—into the Utsira formation 2500 m above the hydrocarbon reservoir [**35**]. The 200-m-thick Utsira is a highly permeable fluid-saturated sandstone capped by the Nordland Shale. Hydrologic and compositional properties of the Utsira are relatively well characterized [**1,4,36**], while those of the Nordland Shale are virtually unknown, and must be estimated [**1,4**].

All of our Sleipner simulations have been carried out within a common 600x250 m spatial domain, which represents the near-field disposal environment, and over a single 20-year time frame, which encompasses equal-duration prograde (active-injection) and retrograde (post-injection) phases. The domain includes a 200-m-thick saline aquifer (35% porosity, 3-darcy permeability), 25-m-thick shale cap rock (5% porosity, 3-microdarcy permeability), and an overlying 25-m-thick saline aquifer. Its lateral boundaries are open to multiphase flow and mass transfer, while its top and bottom boundaries are not. During the prograde phase, pure CO_2 is injected at a rate of 10,000 tons/yr into the basal center of this domain (37^{o}C, 111 bars), which therefore corresponds to a one-m-thick cross-section though the actual 100-m screen length at Sleipner.

Within the common domain, we have evaluated three distinct injection scenarios—models XSH, CSH, and DSH [**1,4**]. Model XSH examines CO_2 injection into a shale-capped homogeneous sandstone aquifer. Models CSH and DSH impose into XSH four thin (3-m thick) intra-aquifer shales, which are separated from the cap rock and each other by 25 m. Model CSH examines the effect of imposing laterally continuous microfractured shales having assigned permeability (3 md) that equates to a continuum representation of 100-μm fractures spaced roughly 30 m apart. Model DSH examines the effect of imposing laterally discontinuous shales, which are bridged by lateral facies change to sandstone. Assigned permeability of these shales (3 μd; same as the cap rock) reflects typical shale integrity.

Compositionally, the well-characterized saline aquifers are represented as impure quartz sand: 80% quartz, 10% K-feldspar, 5% plag-ab_{80}, 3% muscovite, and 2% phlogopite [**1,4**]. The virtually uncharacterized shale cap rock is estimated to contain 60% clay minerals (50% muscovite, 10% Mg-chlorite), 35% quartz, and 5% K-feldspar; this mineralogy and bulk K_2O/(FeO+MgO) ratio closely approximate those of typical (non-carbonaceous) shales, while permitting avoidance of more realistic illite, smectite, and montmorillonite solid solutions, for which thermodynamic and

kinetic data are currently lacking [**1,4**]. Mg end-member components are used to represent Fe/Mg solid solutions because *in situ* oxidation states are unknown. The saline aquifers and shale are all saturated with an aqueous phase of near-seawater composition [1,4,**36**].

Our Sleipner simulations suggest that the ultimate fate of CO_2 injected into saline aquifers is governed by three interdependent yet conceptually distinct processes: CO_2 migration as a buoyant immiscible fluid phase, direct chemical interaction of this rising plume with ambient saline waters, and its indirect chemical interaction with aquifer and cap-rock minerals through the aqueous wetting phase. Each process is directly linked to a corresponding trapping mechanism: immiscible plume migration to hydrodynamic trapping, plume-water interaction to solubility trapping, and plume-mineral interaction to mineral trapping.

Immiscible plume migration and hydrodynamic trapping

Intra-aquifer permeability structure controls the path of prograde immiscible CO_2 migration, thereby establishing the spatial framework of plume-aquifer interaction and the potential effectiveness of solubility and mineral trapping. Actual efficacy of these trapping mechanisms is determined by compositional characteristics of the aquifer and cap rock. By retarding vertical and promoting lateral plume mobility, inter-bedded thin shales significantly expand this framework (i.e., CO_2 storage capacity), enhance this potential, and delay outward migration of the plume from the near-field environment (**Figure 3**). Seismic data strongly suggest that the Utsira formation combines elements of models CSH and DSH (**1,3-4**).

In all three models, steady-state configuration of the immiscible CO_2 plume is realized within one year. During the prograde phase, a residual saturation zone marks the wake of initial plume ascent to the cap rock or deepest inter-bedded shale (e.g., **Figure 3A**, left insets). During the retrograde phase, this zone encompasses virtually the entire prograde steady-state plume (e.g., **Figure 3A**, right inset)—effectively maintaining the prograde extent of solubility trapping and

continually enhancing that of mineral trapping, as described below for model DSH. In the near-field environment of Sleipner-like settings, 80-85% by mass of injected CO_2 remains and migrates as an immiscible fluid phase ultimately subject to hydrodynamic trapping beneath the cap rock, which represents an effective seal in these models[**1-4**], where geomechamical processes are not accounted for.

Geochemical trapping mechanisms

As the immiscible plume equilibrates with saline formation waters, intra-plume aqueous CO_2 concentrations (primarily as $CO_2(aq)$ and HCO_3^-) rapidly achieve their solubility limit, while pH decreases [**1-4**]:

$$CO_2(g) + H_2O = CO_2(aq) + H_2O = HCO_3^- + H^+ \quad (1)$$

For the chemical system and P-T conditions that characterize the Utsira formation at Sleipner, equilibrium aqueous CO_2 solubility is 1.1-1.2 molal, accounting for 15-20% by mass of injected CO_2 (**Figure 4A**). Owing to residual saturation of immiscible CO_2, this degree of solubility trapping is virtually constant throughout the prograde and retrograde phases. The initial pH drop caused by solubility trapping—from 7.1 to 3.4—catalyzes silicate dissolution, which after 20 years has increased pH from 3.4 to 5.3. This dissolution hydrolyzes potential carbonate-forming cations (here, primarily Na, Al, and Mg) within the immiscible-plume source region, and thus represents the critical forerunner of all mineral-trapping mechanisms.

We have identified four distinct mechanisms whereby CO_2 precipitates as carbonate minerals. Intra-plume dawsonite cementation (**Figure 4B**) is catalyzed by high ambient Na^+ concentration, CO_2 influx, and acid-induced K-feldspar dissolution [**1-4**].

$$\underset{\text{K-feldspar}}{KAlSi_3O_8} + Na^+ + CO_2(aq) + H_2O \leftrightarrows \underset{\text{dawsonite}}{NaAlCO_3(OH)_2} + 3\,\underset{\text{silica}}{SiO_2} + K^+ \quad (2)$$

The volume of co-precipitating dawsonite and silica polymorphs slightly exceeds that of dissolving K-feldspar. Hence, this kinetic dissolution/precipitation reaction effectively maintains initial CO_2 injectivity; after 20 years, porosity has decreased by a factor of less than 0.1% (**Figure 5A**). Pervasive dawsonite cementation will likely be characteristic of saline aquifer storage in any feldspathic sandstone. In fact, natural analogs for this process have been documented: widespread dawsonite cement in the Bowen-Gunnedah-Sydney Basin, Eastern Australia, which has been interpreted to reflect magmatic CO_2 seepage on a continental scale [**37**], and sporadic dawsonite cement in the clastic Springerville-St. Johns CO_2 reservoir [**38**].

Calcite-group carbonate rind (here, magnesite) forms along—and therefore effectively delineates—both lateral and upper plume boundaries (**Figure 4C**). Genetically distinct, these two processes can be described by [**1-4**]:

$$Mg^{+2} + CO_2(aq) + H_2O \leftrightarrow \underset{\text{magnesite}}{\underline{MgCO_3}} + 2\,H^+ \qquad (3)$$

As intra-plume formation waters, progressively enriched in Mg^{+2} from phlogopite dissolution, migrate outward across lateral plume boundaries, they traverse steep gradients in CO_2(aq) and pH; the net effect strongly promotes magnesite precipitation. Along upper plume boundaries, CO_2(aq) concentration and pH are nearly constant, but aqueous Mg^{+2} concentration increases most rapidly here because formation-water saturation is minimized; this leads to magnesite cementation from the reservoir/cap-rock interface downward.

However, magnesite precipitation is most extensive from this interface *upwards* (cf. **Figures 4C and 4D**), owing to the relatively high concentration of Mg in clay-rich shales. The coupled intra-shale mineral dissolution/precipitation reaction can be expressed as [**1-4**]:

$$\underset{\text{K-feldspar}}{KAlSi_3O_8} + 2.5\ \underset{\text{Mg-chlorite}}{Mg_5Al_2Si_3O_{10}(OH)_8} + 12.5\ CO_2(aq) \leftrightarrow \underset{\text{muscovite}}{KAl_3Si_3O_{10}(OH)_2} + 1.5\ \underset{\text{kaolinite}}{Al_2Si_2O_5(OH)_4} + 12.5\ \underset{\text{magnesite}}{MgCO_3} + 4.5\ \underset{\text{silica}}{SiO_2} + 6\ H_2O \quad (4)$$

This kinetic reaction proceeds to the right with an increase in solid-phase volume of 18.5% (magnesite accounting for 47 vol.% of the product assemblage). After 20 years, porosity and permeability of the 5-m-thick cap-rock base have been reduced by 8% and 22%, respectively, by this process (**Figure 5B**), which upon hypothetical completion at 130 years would reduce initial porosity by half and initial permeability by an order of magnitude (**Figure 5C**), thereby significantly improving cap-rock integrity. A natural analog to reaction (4) has recently been documented in the Ladbroke Grove natural gas field, where post-accumulation CO_2 influx has converted Fe-rich chlorite to Fe-rich dolomite (ankerite), kaolinite, and silica [**39**].

Although composite mineral trapping accounts for less than 1% by mass of injected CO_2 in our models of the near-field disposal environment at Sleipner, it has enormous strategic significance: it maintains initial CO_2 injectivity (reaction 2), delineates and may partially self-seal plume boundaries (reaction 3), and—most importantly—reduces cap-rock permeability (reaction 4), thereby enhancing hydrodynamic containment of immiscible and solubility-trapped CO_2 [**1-4**].

The CO_2 migration and sequestration processes reviewed above in the context of engineered saline-aquifer storage are equally applicable to CO_2-flood EOR operations in shale-capped water-wet oil reservoirs, which are primarily distinguished by the presence of a hydrocarbon phase and lateral confinement, and the formation of natural CO_2 reservoirs, which are fundamentally distinguished by the rate, focality, and duration of CO_2 influx. However, in all of these settings the effect of geochemical alteration to improve the seal integrity of typical (non-carbonaceous) shale cap rocks may be counterbalanced or even overwhelmed by concomitant geomechanical

deformation, which initially acts in opposition. Hence, in evaluating long-term hydrodynamic sealing capacity, explicit account must be taken of both processes.

Pressure evolution and geomechanical deformation

A first-order assessment of cap-rock geomechanical deformation can be obtained from evaluating the dependence of microfracture aperture evolution on the influx-triggered pressure perturbation. In a new series of NUFT/LDEC simulations, we have assessed this dependence, first as a function of reservoir permeability and lateral continuity—two key parameters that typically distinguish saline-aquifer disposal sites and oil reservoirs, and second, as a function of CO_2 influx rate—the fundamental parameter that distinguishes engineered and natural storage scenarios. Within these new models, the values adopted for other important parameters that influence geomechanical response to CO_2 injection (e.g., reservoir depth and thickness) are those used in the Sleipner simulations described above.

In the Sleipner models, we addressed coupled hydrological and geochemical processes. In the following simulations, we explicitly address only the effect of hydrological (multiphase flow) processes. However, this approximation has negligible impact for impure sandstone reservoirs (such as the Utsira formation), where reservoir porosity and permeability—and thus the injection-induced pressure perturbation—are not modified appreciably by geochemical alteration, as demonstrated above **(Figure 5A**).

Dependence on reservoir properties: saline aquifer versus EOR settings

In this analysis, four distinct simulations have been carried out within two spatial domains (**Figure 6**). Reservoir permeability and lateral continuity are varied from 3000 md and infinite in model UHP (laterally-Unconfined, High Permeability), which represents desirable saline-aquifer storage sites, to 300 md and 2000 m in model CLP (laterally-Confined, Low Permeability), which represents a typical compartmentalized EOR setting. Models ULP and CHP represent cross-combinations of these values, which facilitate evaluation of specific dependence on reservoir

permeability and lateral confinement. In both laterally confined models, compartment height—itself a parameter that exerts second-order influence on the injection-induced pressure perturbation—is 150 m. In all four models, supercritical CO_2 is injected at the rate of 10,000 tons/yr during the prograde event.

Magnitude of the influx-triggered pressure perturbation within basal cap rock varies significantly with (and inversely proportional to) reservoir permeability and lateral continuity (**Figures 7-10**), although the general style of its evolution during prograde and retrograde phases of the influx event does not (**Figure 11**). For highly permeable, laterally extensive reservoirs (model UHP), this perturbation follows a characteristic three-stage evolution: (1) rapid increase to maximum pressure as the aqueous phase is displaced upwards during initial ascent of the immiscible CO_2 plume to the cap rock, (2) rapid asymptotic decrease to a near steady-state value intermediate to ambient and maximum pressures that is maintained thereafter during the prograde regime; and (3) a second rapid asymptotic decrease towards the ambient value, which is triggered by onset of the retrograde regime (**Figure 7**). This pressure evolution suggests that the potential for dependent geomechanical deformation events is maximized during three very brief, distinct episodes that occur during the earliest stages of prograde and retrograde storage. Note that for this Sleipner-like setting, the range of injection-induced pressure variation is small—on the order of 3 bars.

Decreasing reservoir permeability from 3000 to 300 md without imposing lateral confinement (i.e., model ULP) significantly increases magnitude of the pressure perturbation—from roughly 3 to nearly 22 bars—without altering the three-stage evolution described above (cf. **Figures 7 and 8**). Also noteworthy from this comparison is the inverse dependence of CO_2 storage capacity on reservoir permeability, which suggests that for pure-sequestration scenarios the additional energy cost of exploiting less permeable reservoirs—which require higher injection pressures—may be partially offset by the benefit of increased storage and delayed migration into the far-field

environment, providing cap-rock performance is not significantly compromised.

The influence of reservoir compartmentalization on the influx-triggered pressure perturbation within basal cap rock is examined in models CHP and CLP (**Figures 9-10**). Although the functional form of pressure evolution in these models is analogous to that described above for laterally unconfined reservoirs, three significant variations are introduced by compartmentalization. First, the magnitude of initial pressure increase during plume ascent to the cap rock is significantly enhanced—reaching 60 bars in model CLP—owing to the restricted lateral flow (increased flow resistance) of displaced formation water. Second, a permeability-dependent fourth stage of pressure evolution—one that bridges cap-rock and spillpoint plume arrival times—is introduced that either causes a secondary pressure increase (CHP) or slows prograde decrease (CLP) of the initial pressure anomaly. Third, owing to presence of the accumulated CO_2 column, during the retrograde phase pressure decays asymptotically toward a steady-state value that exceeds hydrostatic and whose magnitude is proportional to column height. This final variation is extremely significant because it imposes a long-term pressure increase at and above the cap-rock interface, which does not occur in unconfined reservoirs.

Propagation of the injection-triggered pressure perturbation from the well to and above this interface effects CO_2 migration into undeformed cap rock in cases where its magnitude—more specifically, that of the difference between increased gas and liquid pressures—is sufficient to overcome capillary forces; i.e., capillary entry pressure is exceeded, which permits increased CO_2 saturation within the cap rock as a function of further increased capillary pressure. CO_2 migration into the 25-m-thick 3-μd cap rock through this process is minimized in model UHP, where after 20 years CO_2 saturations of roughly 1% are obtained for a penetration distance of only 5 m, and maximized in model CLP, where CO_2 saturations of about 10% are achieved within this basal 5 m, and penetration distance actually breeches the overlying reservoir, although here CO_2 saturations of <1% are realized (**Figure 12**).

The injection-triggered pressure perturbation also leads to geomechanical deformation of the cap rock, through dependent changes in effective stress and microfracture apertures. Here, we adopt a simplified form of the constitutive relationship between effective stress (σ_E), total stress (σ_T), and pressure (P_f):

$$\sigma_E = \sigma_T - P_f \ , \tag{5}$$

where σ_T is assumed to be constant ($\Delta\sigma_E = -\Delta P_f$). By further neglecting the nonlinear aperture dependence of fracture normal stiffness (K_N), normal aperture displacement due to reduced effective normal stress (Δa_N) can be expressed as:

$$\Delta a_N = (\Delta P_f / K_N). \tag{6}$$

Using equations (5) and (6) together with an estimated normal stiffness for shale fractures at depth [**40**], we first translate the maximum injection-induced pressure perturbation within basal cap rock for each of the four models (**Figure 11**) into the corresponding maximum aperture normal displacement in order to gauge relative scale (**Figure 13**). As can be seen, the potential maximum aperture increase due to reduced effective normal stress is on the order of 100-1000 μm. Because attainment of this pressure maximum coincides with arrival of the immiscible plume at the cap rock—after only 15-100 days in all four models—the potential for geomechanical deformation is maximized very early during the prograde phase.

Simulating long-term aperture evolution requires use of the NUFT-LDEC interface, which facilitates translation of pressure evolution within a given reservoir cap-rock system into the dependent evolution of effective stress and microfracture apertures—here cast within the simplifying context of eqns (5) and (6). In this application, the interface is applied to a representative sub-grid from our NUFT domains: a 60m-by-50m half-space that encompasses the uppermost 10 m of the lower reservoir (2 NUFT grid cells), the 25-m-thick shale cap rock (5 cells),

and the 25-m-thick upper reservoir (5 cells).

The functional form of aperture evolution within basal cap rock is directly analogous to that described above for pressure, as exemplified by LDEC simulation of such evolution for model CLP (**Figure 14**). Here, during the prograde phase apertures rapidly increase by roughly 1000 μm during initial plume ascent, then asymptotically decrease to a steady-state value that reflects net widening of about 400 μm. During the retrograde phase, they first rapidly decrease from this prograde steady state, then continue to decrease asymptotically towards a final steady- state value that reflects ultimate net widening of roughly 100 μm per the approximate 5-bar net pressure increase associated with CO_2 accumulation. Hence, geomechanical deformation degrades cap-rock integrity only during the earliest stages of the prograde phase, after which it continuously self-mitigates this initial degradation eventt.

Unless counterbalanced by geochemical effects, ultimate net aperture widening though geomechanical deformation could facilitate long-term CO_2 migration into the cap rock. Moreover, although maximum prograde and ultimate net aperture increases of 1000 and 100 μm, respectively, occur just above the reservoir interface, concomitant increases of 200-900 and a few 10s of μm, respectively, are realized *throughout* the lowest 20 m of the 25-m-thick shale cap rock (**Figure 15**). Such pervasiveness suggests the potential development of microfracture continuity sufficient to permit CO_2 migration into and perhaps completely through relatively thin shale cap rocks in certain influx settings.

Dependence on influx parameters: engineered versus natural storage

In this analysis, three distinct simulations have been carried out within a single spatial domain (**Figure 16**) that represents a confined sandstone reservoir whose compartment width (10 km), height (100 m), and width:height aspect ratio (100:1) typify those of natural CO_2 reservoirs [**41**].

In all three models, reservoir and shale cap rock permeability are 300 md and 3 μd, respectively. The models are distinguished primarily by prograde CO_2 influx rate, which is varied from 10^4 to 10^3 to 10^2 tons/yr, representing engineered injection, "fast" natural accumulation, and "slow" natural accumulation, respectively. The engineered injection rate is that used in all of the preceeding simulations, while the two values adopted for natural accumulation rates—which are presently unknown [**41**]—are rough estimates. A secondary difference is duration of the prograde and retrograde events, both of which span 10 years for the engineered injection, but are extended to 40 and 20 years in both natural accumulation models.

Because the engineered-injection model adopts the same injection rate used in the preceding set of simulations, it illustrates dependence of the pressure perturbation on compartment width and aspect ratio, while providing a baseline for evaluating its dependence on influx rate per comparison with the two natural accumulation models (**Figure 17**). Increasing compartment width from 2 to 10 km causes pressure to increase even after the plume has reached the cap rock, owing to the increased volume of formation water that must be displaced. Hence, while pressure increases from 90 to 150 bars during initial plume ascent in both models CLP and here (cf. **Figures 10 and 17**), in this case pressure ultimately reaches 250 bars before declining after the plume reaches the lateral compartment boundary. Subsequent asymptotic pressure decline during the post-spillpoint prograde and retrograde phases is dampened by increased compartment width.

When influx rate is reduced by one and two orders of magnitude, migration of the plume is retarded and the pressure perturbation is reduced proportionately, while its functional form remains unchanged (**Figures 18-19**). In the "fast" natural accumulation model, the immiscible plume does not reach the lateral compartment boundary until just before termination of the 40-year prograde event, while the maximum pressure perturbation (about 22 bars) is a factor of 7-8 less than that for the engineered injection model. In the "slow" natural accumulation model, the

plume has not quite advanced halfway to the compartment boundary after 60 years (which encompasses both the prograde and retrograde events), while the maximum pressure perturbation is less than 3 bars.

The extent of CO_2 migration into undeformed shale is strongly dependent on influx rate, through dependence of the injection-triggered pressure perturbation on this rate. Such migration extends halfway through the 25-m-thick shale in the "slow" accumulation model (intra-shale saturations approaching 8%), completely through this shale and halfway through the overlying 25-m-thick reservoir in the "fast" accumulation model (upper reservoir saturations approaching 12%), and completely through this upper reservoir to form a laterally-restricted (see **Figure 17**) accumulation zone beneath the upper domain boundary (where saturations approach 25%) in the engineered injection model (**Figure 20**).

The extent of geomechanical cap-rock deformation through changes in effective stress and dependent aperture evolution is also strongly dependent on influx rate. As the maximum pressure perturbation realized within basal cap rock increases from 3 to 22 to 160 bars with a 10- to 100-fold increase in influx rate (**Figures 17-19**), the dependent aperture widening—evaluated in the context of eqns (5) and (6)—increases from approximately 50 to 350 to 2900 μm.

The three simulations described above address a fundamental question regarding natural CO_2 reservoirs: are they natural analogs to engineered CO_2 storage sites? The models suggest that geomechanical degradation of seal integrity will be characteristic of both natural and engineered CO_2 influx, but significantly more severe during the latter. This result implies that cap-rock isolation performance may vary considerably as a function of filling mode, which further suggests that the currently secure cap rock of a given natural CO_2 accumulation may be incapable of providing an effective seal in the context of an engineered injection. This potential discrepancy

limits the extent to which natural CO_2 reservoirs can be considered directly analogous to engineered CO_2 storage sites.

Geochemical counterbalancing of geomechanical effects

Long-term enhancement or degradation of shale cap-rock integrity ultimately hinges on the relative effectiveness of concomitant geochemical alteration and geomechanical deformation. The analyses presented above offer an opportunity to evaluate an important aspect of this geochemical/geomechanical interplay: the extent to which these initially opposing processes may ultimately counterbalance one another.

This cross-comparison requires a common reference frame, the choices for which are changes in porosity or fracture aperture, which have been used above to represent the respective contributions of geochemical and geomechanical effects. Converting aperture change into the corresponding porosity change requires an initial aperture or fracture density (neither of which are known here), while the aperture change associated with matrix expansion due to a specific mineral dissolution/precipitation reaction can be represented as a function of the dependent variables. Hence, we adopt the latter approach and translate the geochemical contribution into the aperture-change reference frame.

For a given dissolution/precipitation reaction within the matrix, the associated aperture change (Δa) depends on the initial volume fraction of the reactant assemblage (V_R/V_T), standard molal volume change of the reaction ($\Delta V_r^o = V_P^o - V_R^o$), effective diffusion distance (L_D, how deep into matrix blocks the reaction occurs), and reaction progress (C, the extent to which the reaction proceeds towards completion) [**5**]:

$$\Delta a = -2 [(V_R / V_T) (\Delta V_r^o / V_R^o) L_D C] \quad (7)$$

All of these variables are typically known or can be closely estimated except for diffusion distance and reaction progress. Hence, it is both appropriate and convenient to plot Δa isopleths as a function of these latter two parameters.

We have constructed such a diagram for reaction 4 (**Figure 21**), where the Δa-isopleths plotted correspond to the range of geomechanical aperture widening—from initial maximum to final net values (roughly 1000 and 100 μm, respectively)—predicted for model CLP (**Figure 14**). Hence, they can be viewed as geochemical counterbalance isopleths for this most extreme case of the four systems modeled (CLP, CHP, ULP, and UHP); i.e., along any curve, departing to greater diffusion distances or reaction progress equates to net aperture closure (improved cap-rock integrity) as a function of combined geochemical and geomechanical effects, while departing to lesser values equates to net aperture opening (degraded integrity).

This diagram reveals that ultimate geochemical counterbalancing of initial maximum aperture widening (1000 μm) requires diffusion distances of 3-6.5 cm for reaction progress of 30-60%. Moreover, such counterbalancing of the final net widening (100 μm) requires <0.5 cm diffusion distance for the same range of reaction progress; this diffusion length scale and extent of reaction progress—both of which are commonly observed in natural systems—strongly suggest that CO_2 influx-triggered geomechanical deformation may be ultimately counterbalanced by long-term geochemical alteration. This raises the distinct possibility that currently-secure shale cap rocks in natural CO_2 reservoirs may have *evolved* into effective seals following some degree of CO_2 migration through them. Careful mineralogical and petrographic analyses of these shale cap rocks may shed light on this important concept.

Conclusions

Reactive transport and geomechanical models have been interfaced and a new conceptual framework developed to evaluate long-term cap rock integrity in natural and engineered CO_2

storage sites. For typical (non-carbonaceous) shale compositions, influx-triggered geochemical alteration and geomechanical deformation act in opposition to enhance and degrade hydrodynamic seal capacity though aperture narrowing and widening of cap-rock microfractures; hence, net impact of these concomitant processes hinges on their relative effectiveness. The extent of geochemical enhancement is largely independent of reservoir characteristics that distinguish saline-aquifer from EOR/sequestration settings and influx parameters that distinguish engineered disposal sites from natural accumulations, because such characteristics and parameters have negligible (indirect) effect on mineral dissolution/precipitation rates. In contrast, the extent of geomechanical degradation is highly dependent on these reservoir characteristics and influx parameters, because they effectively dictate magnitude of the pressure perturbation. Specifically, it is has been shown inversely proportional to reservoir permeability and lateral continuity and proportional to influx rate.

As a result, while the extent of geochemical alteration is nearly independent of filling mode, that of geomechanical deformation is significantly more pronounced during engineered storage. This suggests that the currently secure cap rock of a given natural CO_2 accumulation may be incapable of providing an effective seal in the context of engineered injection, a potential discrepancy that limits the extent to which natural CO_2 reservoirs and engineered storage sites can be considered analogous. In addition, the pressure increase associated with CO_2 accumulation in any compartmentalized system invariably results in net geomechanical aperture widening of cap-rock microfractures. This suggests that ultimate restoration of pre-influx hydrodynamic sealing capacity—in both EOR/sequestration and natural accumulation settings—hinges on ultimate geochemical counterbalancing of this geomechanical effect, which further suggests that the well documented leaky-to-secure character of fossil CO_2 reservoirs may reflect the incomplete-to-complete nature of such restoration.

To explore these hypotheses, a new conceptual framework has been introduced that depicts ultimate geochemical counterbalancing of geomechanical aperture evolution as a function of effective diffusion distance and reaction progress. This framework reveals diffusion length scales and reaction progress extents consistent with those observed in nature, which suggests that ultimate counterbalancing of geochemical and geomechanical effects is feasible, and, therefore, that shale cap rocks may in fact *evolve* into effective seals—in both natural and engineered storage sites. Further, it provides a theoretical model for assessing the extent to which cap-rock integrity will ultimately be enhanced or degraded in specific reservoir/cap-rock systems in the context of specific engineered injection scenarios.

Recommendations

The present contribution can be viewed as a scoping study in which influx-triggered geochemical and geomechanical contributions to cap-rock integrity have been modeled, then merged within a new conceptual framework that facilitates assessment of their ultimate net effect for CO_2 storage sites whose compositional and influx parameters can be well characterized. As such, it provides a unique computational methodology for addressing two central issues for geologic storage—long-term prediction of isolation performance and the extent to which natural and engineered sites are analogous. A number of model development and application activities are immediately posed by this inaugural work.

In terms of important technological advances, there is a pressing need to develop a simulation capability that fully integrates reactive transport and geomechanical processes, which we have merely interfaced here. There are many ways to accomplish this, ranging from, ideally, a global-implicit approach to, perhaps more realistically in the short-term, bi-directional coupling of distinct models. Equally pressing is the need for improved kinetic descriptions of mineral dissolution and (especially) precipitation processes as well as more accuate and comprehensive databases of

the associated species-specific parameters; these developments will lead to improved predictive capabilities. Also very important is the need to develop methodology for assessing the specifc rates and time frames of geochemical counterbalancing that involves multiple dissolution/precipitation reactions; here, we have addressed this concept only in a time-integrated sense and for a single representative reaction.

In parallel with such development activities, several key applications could provide critical benchmarking, validation, and refinement for both the simulation capabilities and new hypotheses described above. For example, detailed reactive transport modeling of well-characterized fossil or active CO_2 reservoirs—ideally, a suite of leaky-to-secure systems for which cap-rock core is available—would provide a crucial field-scale test bed for the incomplete-to-complete geochemcial counterbalancing concept. Similarly detailed modeling of carefully designed and precisely characterized batch and plug-flow reactor experiments would provide an analogous laboratory-scale test bed for this theory—as well as the ideal means of benchmarking simulation capabilities for all mineral trapping mechanisms.

Closely integrated modeling/experimental studies such as these—on both the field and laboratory scale—also provide an effective methodology for evaluating key compositional dependencies of long-term cap rock (and reservoir) integrity. Such dependencies include those associated with formation waters (e.g. salinity, specific cation/anion concentrations) and waste-stream impurities (e.g., CH_4, H_2S, SO_x,NO_x concentrations) as well as the effect of lithologic diversity, ranging from the influence of carbonate cements on the shale-capped sandstone systems addressed here to a dramatic shift from such environments into, for example, anhydrite-capped carbonate reservoirs.

Finally, for a suite of well-characterized potential CO_2 disposal sites, reactive transport and geomechanical modeling could be used to identify and evaluate the volume change associated with key injection-triggered mineral dissolution/precipitation reactions, to assess concomitant

pressure-dependent geomechanical deformation, and to determine net impact of these interdependent processes on long-term cap-rock integrity (e.g., Figure 21). It would be particularly instructive and useful to carry out this modeling study for a suite of prospective sites that spans the broad range of potential reservoir/cap-rock lithologies—well beyond the single sandstone/shale combination examined here. Such an analysis would provide a unique means of quantitatively ranking long-term isolation performance as a function of important lithologic and other dependent variations.

Acknowledgements

This work was performed under the auspices of the U.S. Department of Energy by University of California, Lawrence Livermore National Laboratory under Contract W-7405-Eng-48. Funding support was provided by the JIP CO_2 Capture Project and the U.S. Department of Energy (Office of Fossil Energy) through a CRADA (TC-02038). It is a pleasure to thank Associate Editor Curt Oldenburg and two anonymous reviewers for their critiques of the original manuscript; each contributed a number of comments that were invaluable in preparing the revised contribution.

References

[1] Johnson, J.W., Nitao, J.J., Steefel, C.I., and Knauss, K.G., 2001, Reactive transport modeling of geologic CO_2 sequestration in saline aquifers: the influence of intra-aquifer shales and the relative effectiveness of structural, solubility, and mineral trapping during prograde and retrograde sequestration. Proc. First Natl. Conf. Carbon Sequestration, Washington, DC, May 14-17, 2001, 60 p.

[2] Johnson, J.W., Nitao, J.J., and Steefel, C.I., 2002a, Fundamental elements of geologic CO_2 sequestration in saline aquifers: Amer. Chem. Soc., Fuel Chem. Div. Preprints, v. 47, n. 1, p. 41-42.

[3] Johnson, J.W., and Nitao, J.J., 2002b, Reactive transport modeling of geologic CO_2 sequestration at Sleipner: Proc. Sixth Intl. Conf. Greenhouse Gas Control Technologies (GHGT-6), Kyoto, Japan, Oct 1-4, 2002, v. 1, p. 327-332.

[4] Johnson, J.W., Nitao, J.J., and Knauss, K.G., 2004, Reactive transport modeling of CO_2 storage in saline aquifers to elucidate fundamental processes, trapping mechanisms, and sequestration partitioning: Geol. Soc. London Spec. Pub. “Geologic Storage of carbon dioxide for emissions reduction: Technology”, Baines, S.J., and Worden, R.H., and eds. (in press).

[5] Johnson, J.W., Nitao, J.J., Morris, J.P., and Blair, S.C., 2003a, Reactive transport modeling of geohazards associated with offshore CO_2 injection for EOR and geologic sequestration: Proc. Offshore Technology Conf., Houston, TX, May 5-8, 2003, 9 p.

[6] Johnson, J.W., Nitao, J.J., and Morris, J.P., 2003b, Reactive transport modeling of long-term cap rock integrity during CO_2 injection for EOR or saline-aquifer storage: Second Natl. Conf. Carbon Sequestration, Alexandria, VA, May 5-8, 2003.

[7] Johnson, J.W., Nitao, J.J., Morris, J.P., and Blair, S.C., 2003c, CO_2 reservoirs: are they natural analogs to engineered geologic storage sites?: AAPG Annual Meeting, Salt Lake City, UT, May 11-14, 2003.

[8] Johnson, J.W., Nitao, J.J., and Morris, J.P., 2003d, Reactive transport modeling of cap rock integrity during natural and engineered CO_2 sequestration: Amer. Chem. Soc. Natl. Meeting, New York, NY, September 7-11, 2003.

[9] Wildenborg, T., 2004, Safety assessment methodology for carbon dioxide sequestration (SAMCARDS) [replace with actual ms title]: CCP Summary Vol. 2.

[10] Stevens, S.H., 2004, Natural analogs for geologic CO_2 sequestration [replace with actual ms title]: CCP Summary Vol. 2.

[11] Borm, G., Schutt, H., Spangenberg, E., et al., 2004, Influence of CO_2 injection on the physical properties of reservoir and cap rocks [replace with actual authorship and ms title]: CCP Summary Vol. 2.

[12] Nimz, G.J., and Hudson, G.B., 2004, Noble isotopes for screening, monitoring, and verification at CO_2 storage sites [replace with actual ms title]: CCP Summary Vol. 2.

[13] Hoversten, G.M., and Gasperikova, E., 2004, Novel geophysical techniques for monitoring CO_2 migration [replace with actual ms title]: CCP Summary Vol. 2.

[14] Evans, J., Shipton, Z., et al., 2004, Geological and Geochemical Analyses of leakage of naturally charged CO_2 reservoirs: Implications for CO_2 sequestration strategies [replace with actual authorship and ms title]: CCP Summary Vol. 2.

[15] Norton, D., 1984, Theory of hydrothermal systems: Ann. Rev. Earth Planet.Sci., v. 12, p. 155-177.

[16] Johnson, J.W., Nitao, J.J., Tompson, A.F.B., Steefel, C.I., *et al*., 1999, 21st-century tools for modeling reactive transport in dynamic geologic systems of economic and environmental significance: in Earth and Environmental Sciences 1998 Annual Report, p. 7-11, LLNL, UCRL-LR-126434-98.

[17] Bertrand, C., Fritz, B., and Sureau, J.F., 1994, Hydrothermal experiments and thermo-kinetic modelling of water-sandstone interactions: Chem. Geol., v. 116, p. 189-192.

[18] Johnson, J.W., Knauss, K.G., Glassley, W.E., and DeLoach, L.D., and Tompson, A.F.B., 1998, Reactive transport modeling of plug-flow reactor experiments: quartz and tuff dissolution at 240^{o}C: J. Hydrology, v. 209, p. 81-111.

[19] Nitao, J.J., 1998a, Reference manual for the NUFT flow and transport code, version 2.0: LLNL, UCRL-MA-130651, 55 p.

[20] Nitao, J.J., 1998b, User's manual for the USNT module of the NUFT Code, Version 2.0 (NP-Phase, NC-component, Thermal): LLNL, UCRL-MA-130653, 76 p.

[21] Parker, J.C., Lenhard, R.J., and Kuppusamy, T., 1987, A parametric model for constitutive properties governing multiphase flow in porous media: Water Resources Research, v. 23, n. 4, p. 618-624.

[22] Lasaga, A.C., 1998, Kinetic Theory in the Earth Sciences: Princeton Univ. Press, Princeton, NJ, 811 p.

[23] Scheidegger, A.E., 1974, The Physics of Flow through Porous Media (3rd ed.): Univ. Toronto Press, Toronto, 353 p.

[24] Johnson, J.W., and Lundeen, S.R., 1994a, Jewel: A graphical-user interface for generating custom GEMBOCHS thermodynamic datafiles for use with geochemical modeling software: LLNL-YMP Milestone report MOL63, 23 p.

[25] Johnson, J.W., and Lundeen, S.R., 1994b, GEMBOCHS thermodynamic datafiles for use with the EQ3/6 software package: LLNL-YMP Milestone report MOL72, 99 p.

[26] Johnson, J.W., Oelkers, E.H., and Helgeson, H.C., 1992, SUPCRT92: A software package for calculating the standard molal thermodynamic properties of minerals, gases, aqueous species, and reactions from 1 to 5000 bars and 0 to 1000C: Comp. Geosci., v. 18, n. 7, p. 899-947.

[27] Shock, E.L., 1998, An updated and augmented version (slop98.dat) of the original SUPCRT92 database (sprons92.dat) is available on the Dr. Shock's website: http://zonvark.wustl.edu/geopig/

[28] Johnson, J.W., and Norton, D., 1991, Critical phenomena in hydrothermal systems: State, thermodynamic, electrostatic, and transport properties of H_2O in the critical region: Amer. J. Sci., v. 291, pp. 541-648.

[29] Tanger, J.C. IV, and Helgeson, H.C., 1988, Calculation of the thermodynamic and transport properties of aqueous species at high pressures and temperatures: Revised equations of state for the standard partial molal properties of ions and electrolytes: Amer. J. Sci., v. 288, n. 1, p. 19-98.

[30] Shock, E.L., Oelkers, E.H., Johnson, J.W., Sverjensky, D.A., and Helgeson, H.C., 1992, Calculation of the thermodynamic properties of aqueous species at high pressures and temperatures: Effective electrostatic radii, dissociation constants, and standard partial molal properties to 1000C and 5 kb: J. Chem. Soc. (London) Faraday Trans., v. 88, n. 6, p. 803-826.

[31] Helgeson, H.C., Delany, J.M, Nesbitt, H.W., and Bird, D.K., 1978, Summary and critique of the thermodynamic properties of rock-forming minerals: Amer. J. Sci., v. 278-A, 229 p.

[32] Morris, J.P., Glenn, L.A., and Blair, S.C., 2002, The distinct element method—application to structures in jointed rock: Lecture Notes Computational Science and Engineering, v. 26, p. 291-306.

[33] Morris, J.P., Rubin, M.B, Blair, S.C., Glenn, L.A., and Heuze, F.E., 2004, Simulations of underground structures subjected to dynamic loading using the distinct element method: Engineering Computations (in press).

[34] Cundall, P.A., 1988, Formulation of a three-dimensional distinct element model—Part I: A scheme to detect and represent contacts in a system composed of many polyhedral blocks: Int. J. Rock Mech. Min. Soc. & Geomech. Abstr., v. 25. p. 107-116.

[35] Torp, T.A., and Gale, J., 2002, Demonstrating storage of CO_2 in geological reservoirs: the Sleipner and SACS projects: Proc. Sixth Intl. Conf. Greenhouse Gas Control Technologies (GHGT-6), Kyoto, Japan, Oct 1-4, 2002.

[36] Gregersen, U., et al., 1998, "SACS Phase Zero Report" (provided courtesy of SACS).

[37] Baker, J.C., Bai, G.P., Hamilton, P.J., Golding, S.D., and Keene, J.B., 1995, "Continental-scale magmatic carbon-dioxide seepage recorded by dawsonite in the Bowen-Gunnedah-Sydney Basin, Eastern Australia", J. Sed. Res., v. 65, n. (3), p. 522-530.

[38] Moore, J., Adams, M., Allis, R., Lutz, S., and Rauzi, S., 2003, Investigations of CO_2 mobility in natural reservoirs beneath the Colorado Plateau and Southern Rocky Mountains, Proc. Second Ann. Conf. Carbon Sequestration, May 5-8, 2003, Alexandria, Virginia, 22 p.

[39] Watson, M.N., Zwingmann, N., and Lemon, N.M., 2002, "The Ladbroke Grove-Katnook carbon dioxide natural laboratory: A recent CO_2 accumulation in a lithic sandstone reservoir", Proc. Sixth Intl. Conf. Greenhouse Gas Control Technologies (GHGT-6), Kyoto, Japan, Oct 1-4, 2002, v. 1, p. 435-440.

[40] Bilgin, H.A., and Pasamehmetoglu, A.G., 1990, "Shear behaviour of shale joints under heat in direct shear", in *Rock Joints*, Barton, N., and Stephansson, O., eds., 179-183.

[41] Allis, R., Chidsey, T., Gywnn, W., Morgan, C., White, S., Adams, M., and Moore, J., 2001, Natural CO_2 Reservoirs on the Colorado Plateau and Southern Rocky Mountains: Candidates for CO_2 Sequestration: Proc. First Natl. Conf. Carbon Sequestration, Washington, DC, May 14-17, 2001, 19 p.

List of Acronyms and Abbreviations

CCP	CO_2 Capture Project
GEMBOCHS	Geologic and Engineering Materials: Bibliography Of Chemical Species (Thermodynamic/kinetic database and software library [24-25])
LDEC	Livermore Distinct Element Code (geomechanical modeling software [32-33])
NUFT	Non-isothermal Unsaturated Flow and Transport (reactive transport software [19-20])
SUPCRT92	SUPerCRiTical (geochemical modeling software and database: [26])

Figure Captions

Figure 1: Schematic depiction of coupled subsurface processes that redistribute mass and energy in response to natural or engineered perturbation events. Porosity and permeability are the key variables that link hydrological, geochemical, and geomechanical sectors of the diagram.

Figure 2: Schematic depiction of concomitant CO_2 influx-triggered geochemical and geomechanical processes within shale cap rock microfractures. Mineral dissolution/precipitation reactions tend to continuously reduce microfracture apertures for typical shale compositions, while pressure evolution initially widens then reduces them (net widening).

Figure 3: Immiscible plume migration and hydrodynamic trapping after 3 years in Sleipner models XSH, CSH, and DSH; interbedded thin shales not shown for CSH and DSH.

Figure 4: Geochemical trapping mechanisms after 20 years in model DSH: (A) solubility trapping (composite molality of all carbon-bearing aqueous species) , (B) intra-plume dawsonite cementation, (C) plume-bounding magnesite precipitation (shales shown in white [off-scale high]), and (D) intra-shale magnesite precipitation.

Figure 5: Porosity and permeability reduction in model DSH due to mineral trapping (A) after 20 years in the reservoir (initial porosity:35%; shales shown in white [off-scale low]) and (B-C) after 20 and 130 years in the cap rock.

Figure 6: Schematic depiction of the laterally unconfined and laterally confined simulation domains used for models UHP/ULP and CHP/CLP, respectively. Illustrated basal cap rock and CO_2 injection cells are not drawn to scale. Actual cell granularity is overlain upon the hydrostatic gradient plot , which is identical in the two systems (shown for models CHP/CLP).

Figure 7. NUFT simulation of immiscible CO_2 migration together with associated pressure evolution within the basal cap rock directly above and as a function of distance from CO_2 injection for the laterally unconfined 3000 md reservoir.

Figure 8. NUFT simulation of immiscible CO_2 migration together with associated pressure evolution within the basal cap rock directly above and as a function of distance from CO_2 injection for the laterally unconfined 300 md reservoir.

Figure 9. NUFT simulation of immiscible CO_2 migration together with associated pressure evolution within the basal cap rock directly above and as a function of distance from CO_2 injection for the laterally confined 3000 md reservoir.

Figure 10. NUFT simulation of immiscible CO_2 migration together with associated pressure evolution within the basal cap rock directly above and as a function of distance from CO_2 injection for the laterally confined 300 md reservoir.

Figure 11: NUFT simulation of pressure evolution within the basal cap rock directly above CO_2 injection for models UHP, ULP, CHP, and CLP together with the distance profiles associated with attainment of pressure maxima (inset).

Figure 12. NUFT simulation of CO_2 migration into geomechanically undeformed cap rock as a function of the CO_2 influx-induced pressure perturbation, which in models UHP, ULP, CHP, and CLP (shown from left to right) is sufficient to overcome resistive capillary forces.

Figure 13: Maximum potential aperture increase of basal cap rock microfractures as a function of the CO_2 influx-triggered initial pressure increase and reduced effective normal stress in models UHP, ULP, CHP, and CLP.

Figure 14. LDEC simulation of microfracture aperture evolution in the basal cap rock directly above the CO_2 injection well in model CLP.

Figure 15. LDEC simulation of aperture evolution within and immediately surrounding the cap rock in model CLP.

Figure 16: Schematic depiction of the laterally confined simulation domain used to represent natural CO_2 reservoirs. Illustrated basal cap rock and CO_2 influx cells are not drawn to scale. Actual cell granularity is overlain upon the hydrostatic gradient plot.

Figure 17. NUFT simulation of immiscible CO_2 migration together with associated pressure evolution within the basal cap rock directly above and as a function of distance from CO_2 injection for engineered injection.

Figure 18. NUFT simulation of immiscible CO_2 migration together with associated pressure evolution within the basal cap rock directly above and as a function of distance from CO_2 influx for "fast" natural accumulation.

Figure 19. NUFT simulation of immiscible CO_2 migration together with associated pressure evolution within the basal cap rock directly above and as a function of distance from CO_2 influx for "slow" natural accumulation.

Figure 20. NUFT simulation of CO_2 migration into geomechanically undeformed cap rock as a function of the influx-triggered pressure perturbation, which in the "slow" and "fast" natural accumulation and engineered injection models (shown from left to right) is sufficient to overcome resistive capillary forces.

Figure 21. Conceptual framework for assessing potential long-term geochemical counterbalancing of geomechanical effects: geochemical Δaperture isopleths plotted as a function of diffusion distance and reaction progress for mineral dissolution/precipitation reaction (4), where ΔV_r^o is +18.5% and V_R/V_T is 0.1425, constructed using reaction (7) over the range of geomechanical Δaperture defined by initial maximum and ultimate net widening for model CLP (Figure 14).

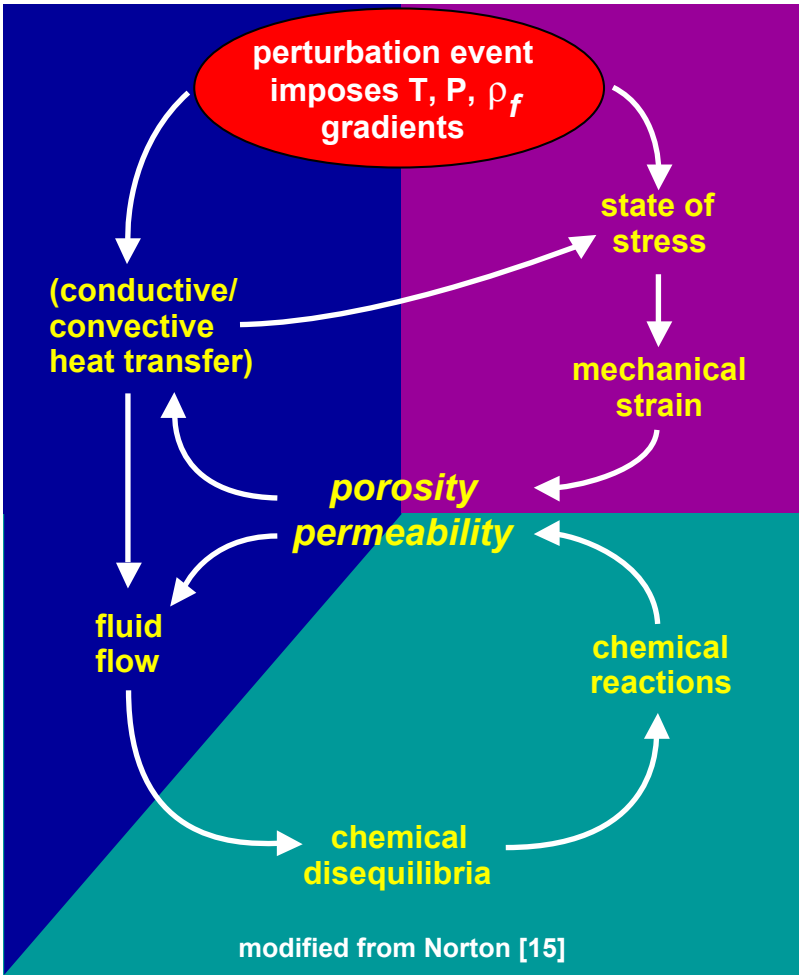
perturbation event
imposes T, P, ρ_f
gradients
state of
stress
(conductive/
convective
heat transfer)
mechanical
strain
porosity
permeability
fluid
flow
chemical
reactions
chemical
disequilibria
modified from Norton [15]

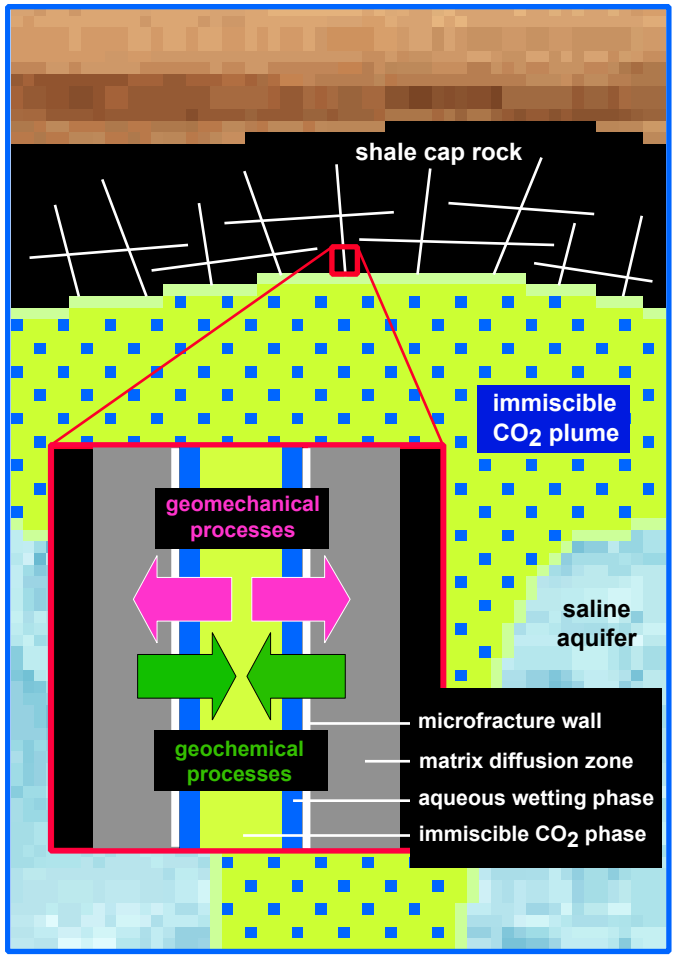
shale cap rock
immiscible
CO_2 plume
geomechanical
processes
saline
aquifer
geochemical
processes
microfracture wall
matrix diffusion zone
aqueous wetting phase
immiscible CO_2 phase

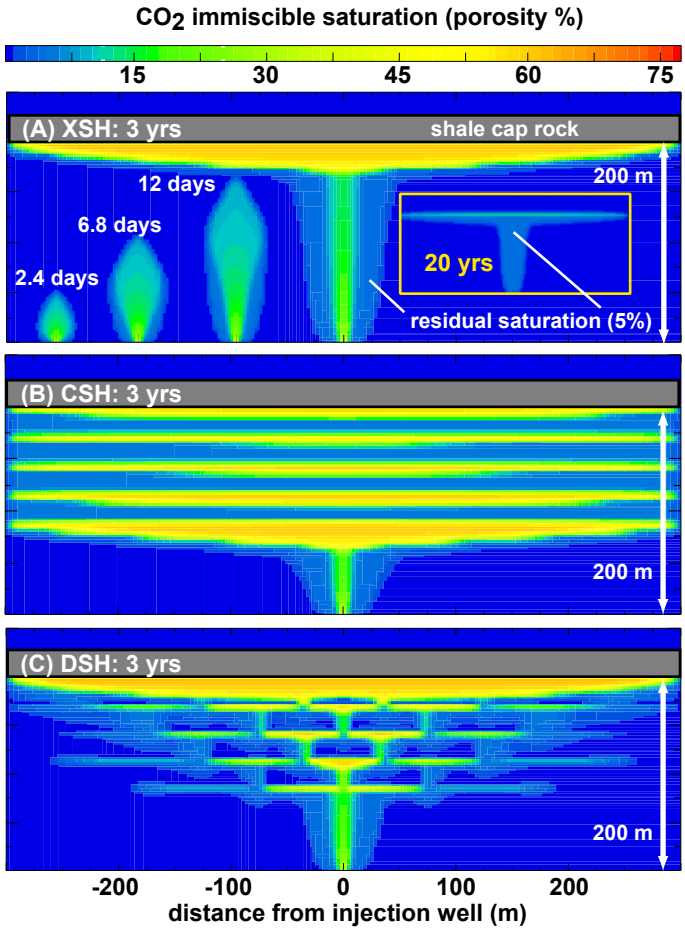
CO2 immiscible saturation (porosity %)
15
30
45
60
75
(A) XSH: 3 yrs
shale cap rock
12 days
6.8 days
2.4 days
200 m
20 yrs
residual saturation (5%)
(B) CSH: 3 yrs
200 m
(C) DSH: 3 yrs
200 m
-200
-100
0
100
200
distance from injection well (m)

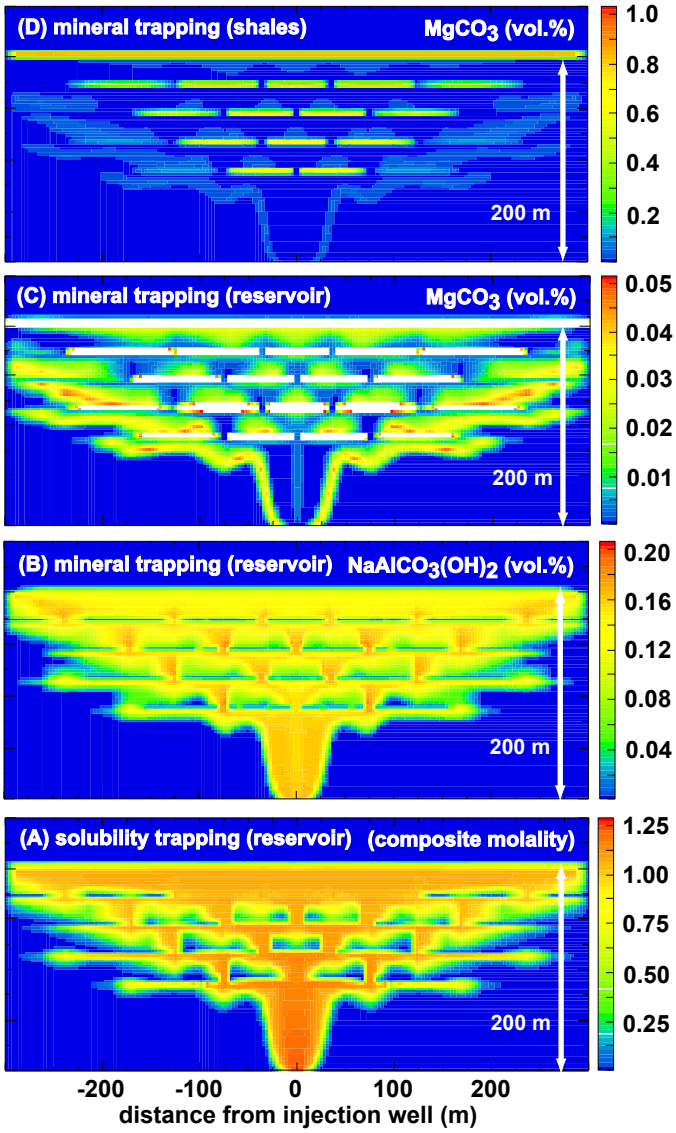
(D) mineral trapping (shales)
MgCO3 (vol.%)
200 m
1.0
0.8
0.6
0.4
0.2
(C) mineral trapping (reservoir)
MgCO3 (vol.%)
200 m
0.05
0.04
0.03
0.02
0.01
(B) mineral trapping (reservoir)
NaAlCO3(OH)2 (vol.%)
200 m
0.20
0.16
0.12
0.08
0.04
(A) solubility trapping (reservoir)
(composite molality)
200 m
1.25
1.00
0.75
0.50
0.25
-200
-100
0
100
200
distance from injection well (m)

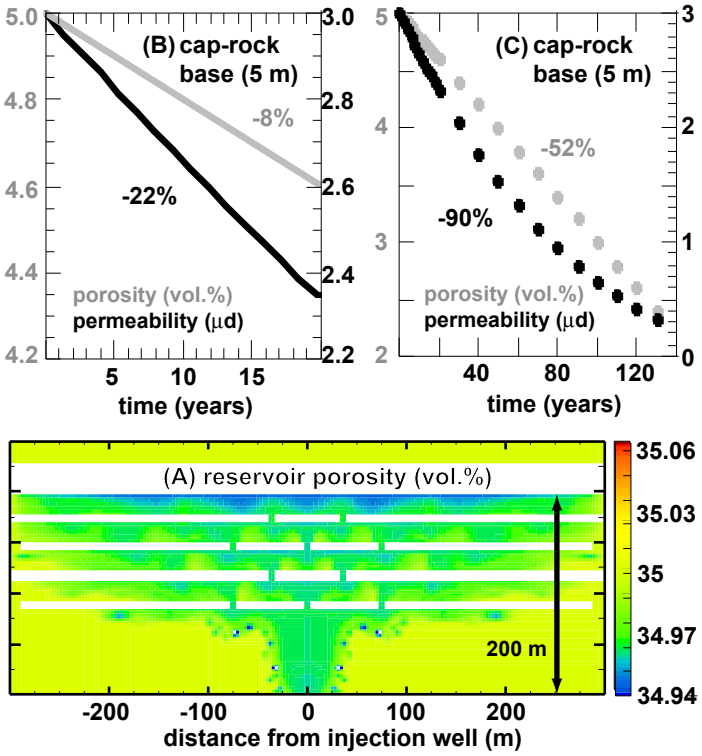
(B) cap-rock
base (5 m)
-8%
-22%
porosity (vol.%)
permeability (μd)
time (years)
(C) cap-rock
base (5 m)
-52%
-90%
porosity (vol.%)
permeability (μd)
time (years)
(A) reservoir porosity (vol.%)
200 m
distance from injection well (m)

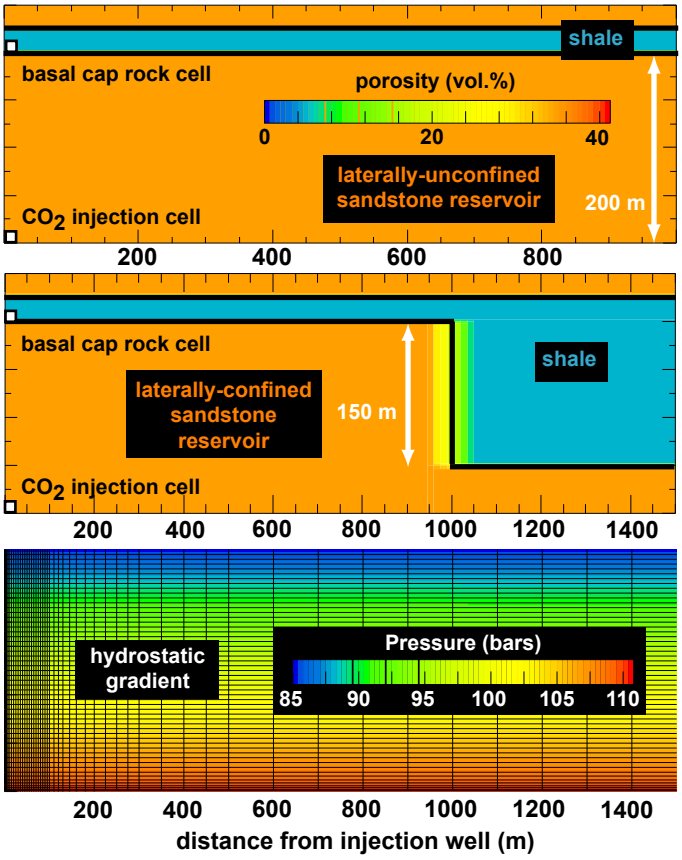
shale
basal cap rock cell
porosity (vol.%)
0
20
40
laterally-unconfined
sandstone reservoir
200 m
CO2 injection cell
200
400
600
800
basal cap rock cell
laterally-confined
sandstone
reservoir
150 m
shale
CO2 injection cell
200
400
600
800
1000
1200
1400
hydrostatic
gradient
Pressure (bars)
85
90
95
100
105
110
200
400
600
800
1000
1200
1400
distance from injection well (m)

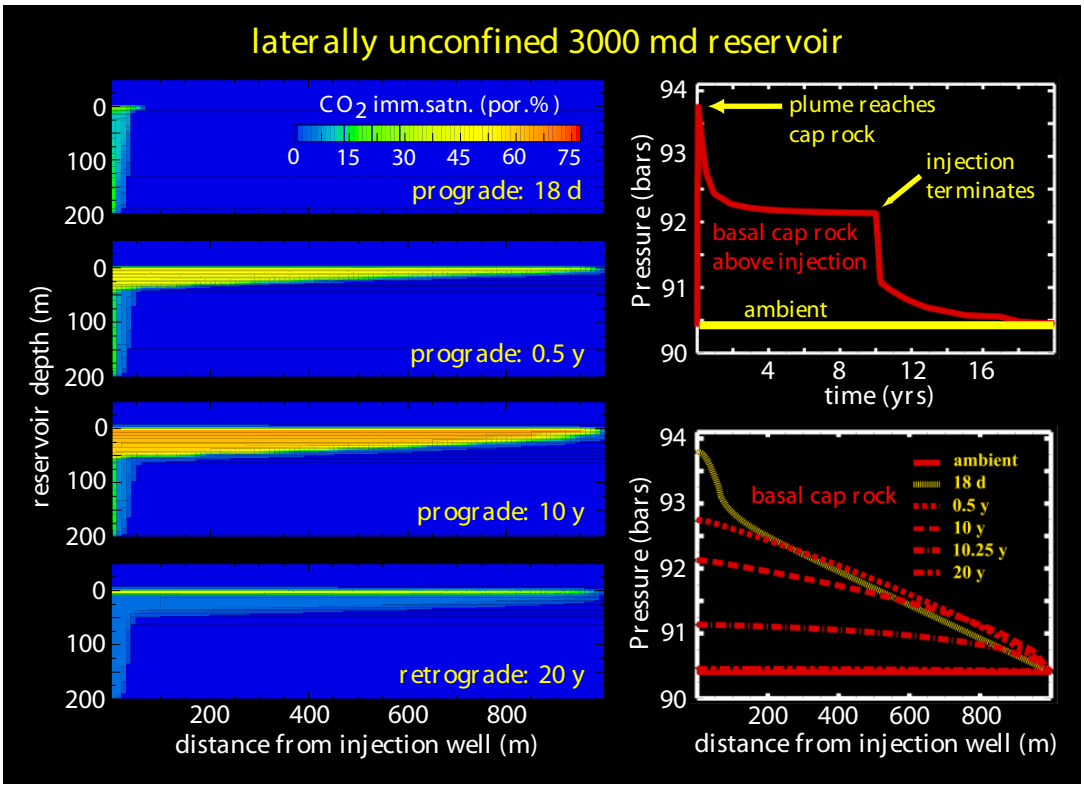
laterally unconfined 3000 md reservoir
CO2 imm.satn. (por.%)
0 15 30 45 60 75
prograde: 18 d
prograde: 0.5 y
prograde: 10 y
retrograde: 20 y
reservoir depth (m)
0
100
200
distance from injection well (m)
plume reaches cap rock
injection terminates
basal cap rock above injection
ambient
Pressure (bars)
time (yrs)
basal cap rock
ambient
18 d
0.5 y
10 y
10.25 y
20 y

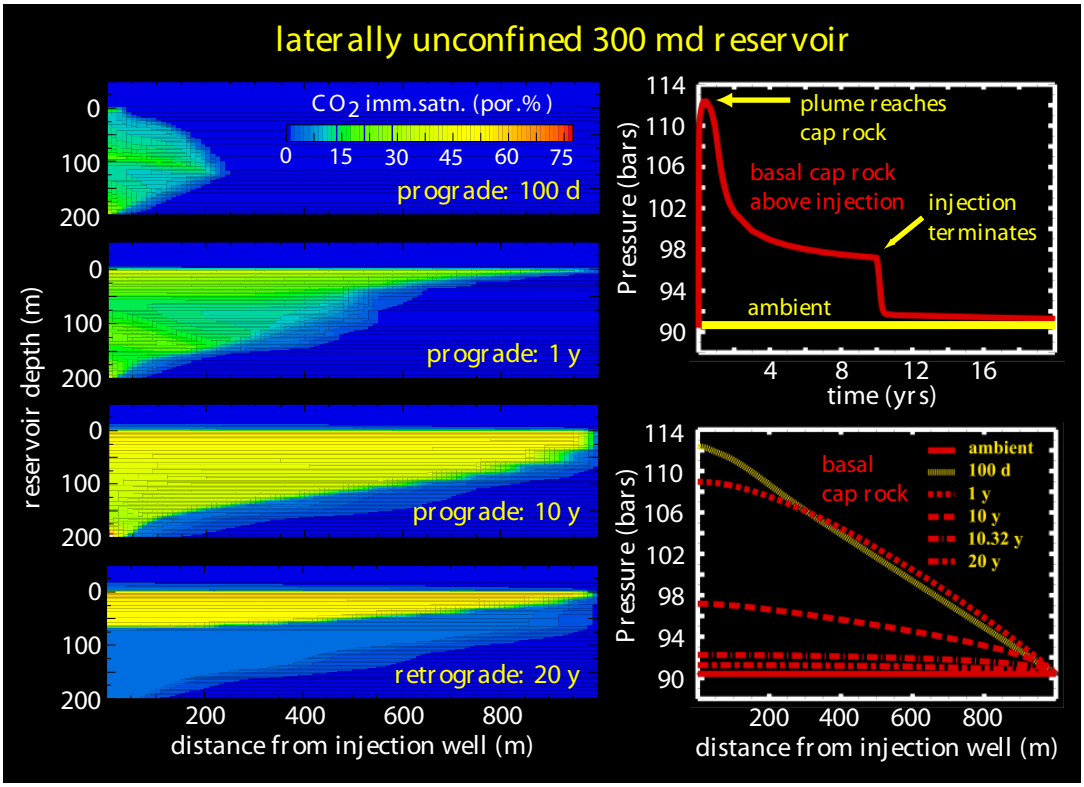
laterally unconfined 300 md reservoir
CO2 imm.satn. (por.%)
0 15 30 45 60 75
prograde: 100 d
prograde: 1 y
prograde: 10 y
retrograde: 20 y
reservoir depth (m)
0
100
200
200 400 600 800
distance from injection well (m)
Pressure (bars)
114 110 106 102 98 94 90
plume reaches cap rock
basal cap rock above injection
injection terminates
ambient
4 8 12 16
time (yrs)
basal cap rock
ambient
100 d
1 y
10 y
10.32 y
20 y
200 400 600 800
distance from injection well (m)

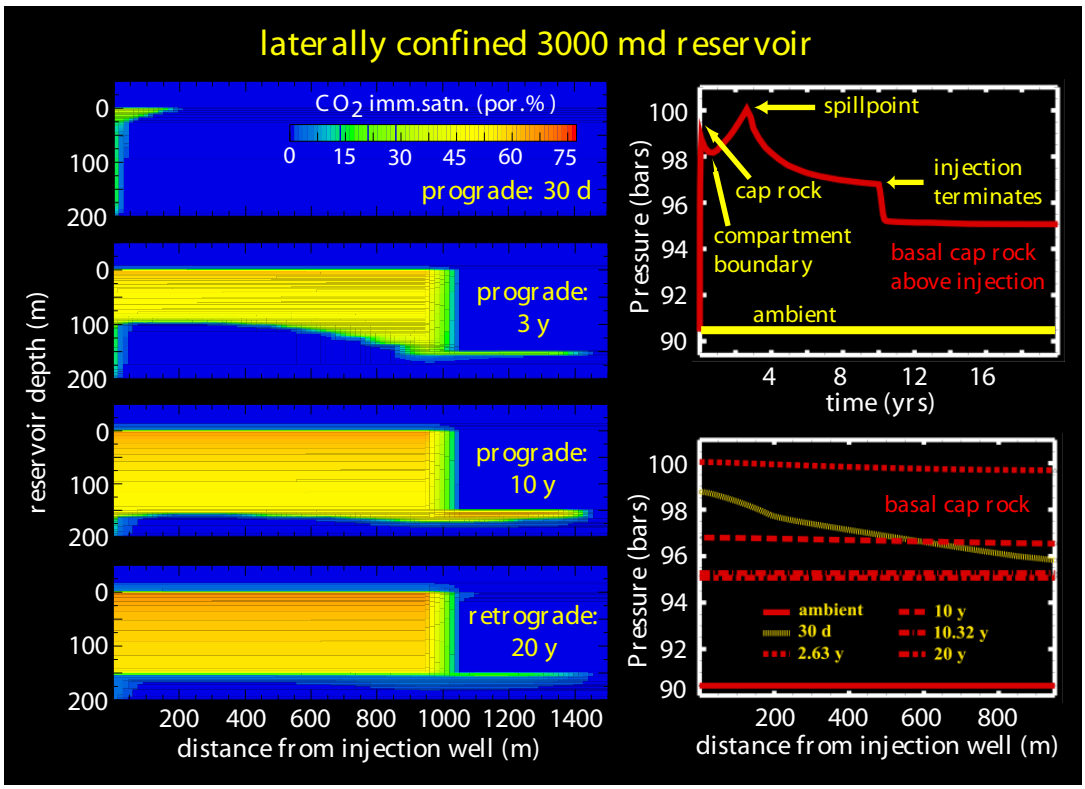
laterally confined 3000 md reservoir
CO_2 imm.satn. (por.%)
0 15 30 45 60 75
prograde: 30 d
prograde: 3 y
prograde: 10 y
retrograde: 20 y
reservoir depth (m)
0
100
200
200 400 600 800 1000 1200 1400
distance from injection well (m)
spillpoint
cap rock
injection terminates
compartment boundary
basal cap rock above injection
ambient
Pressure (bars)
100
98
96
94
92
90
4 8 12 16
time (yrs)
basal cap rock
ambient
30 d
2.63 y
10 y
10.32 y
20 y
200 400 600 800
distance from injection well (m)

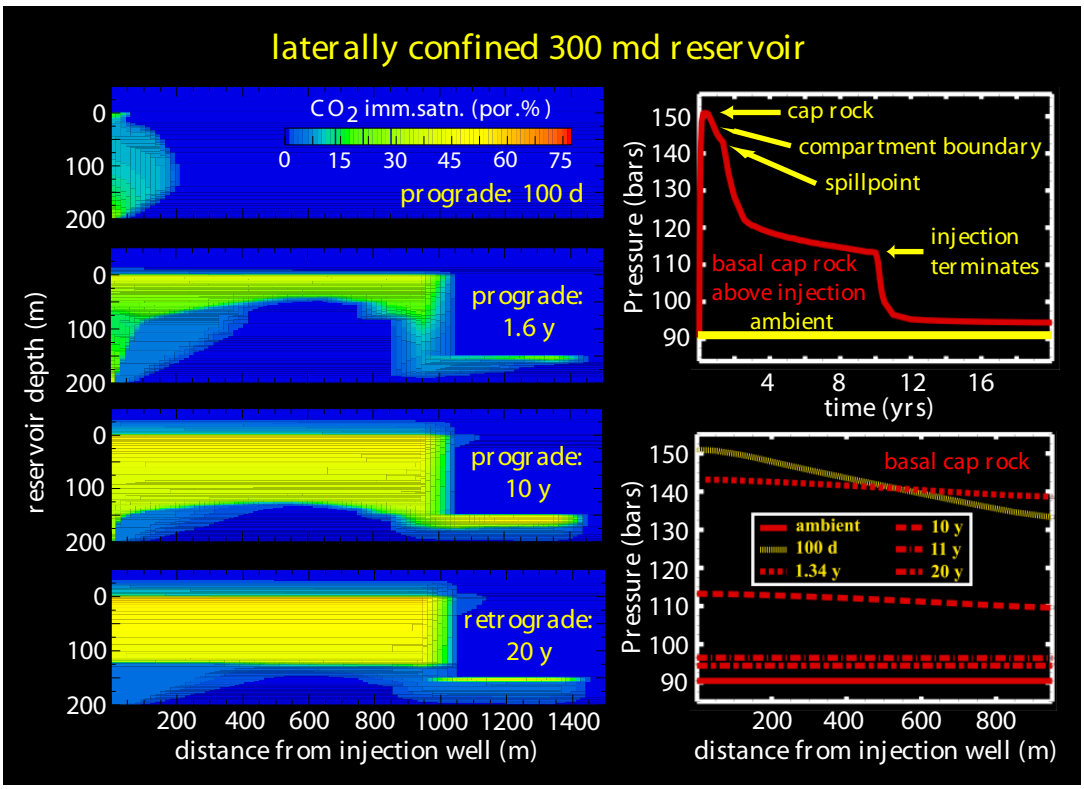
laterally confined 300 md reservoir
CO2 imm.satn. (por.%)
0 15 30 45 60 75
prograde: 100 d
prograde: 1.6 y
prograde: 10 y
retrograde: 20 y
reservoir depth (m)
0
100
200
200 400 600 800 1000 1200 1400
distance from injection well (m)
cap rock
compartment boundary
spillpoint
injection terminates
basal cap rock above injection
ambient
Pressure (bars)
150 140 130 120 110 100 90
4 8 12 16
time (yrs)
basal cap rock
ambient
100 d
1.34 y
10 y
11 y
20 y
200 400 600 800
distance from injection well (m)

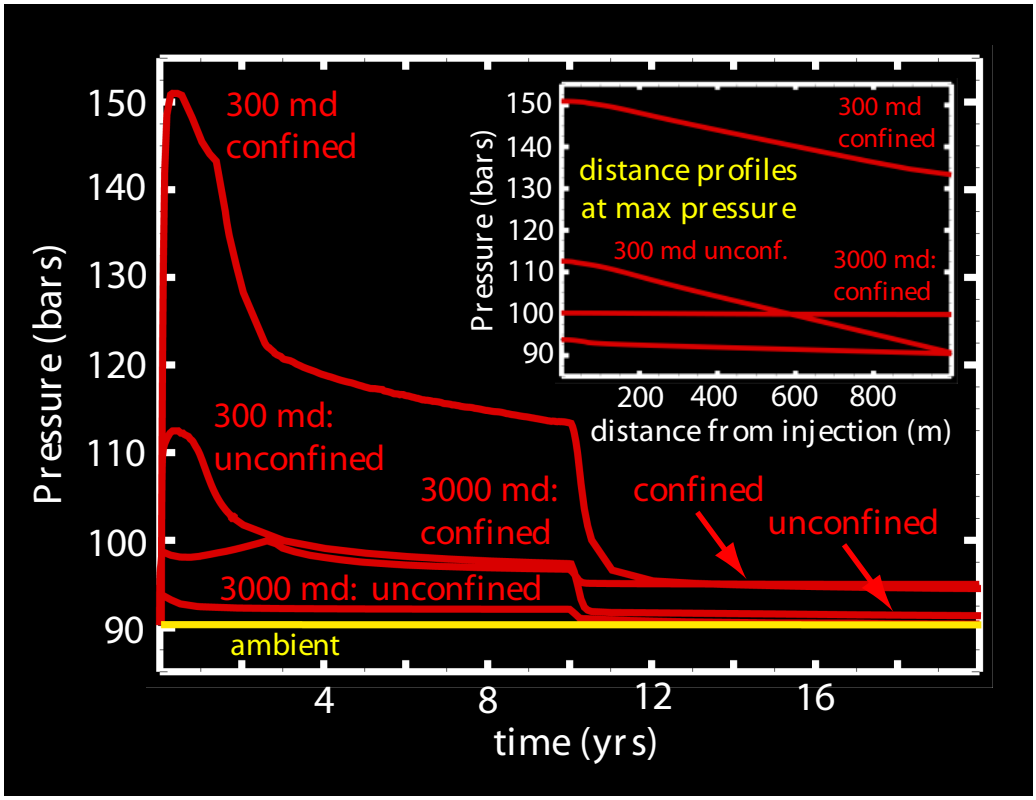
Pressure (bars)
150
140
130
120
110
100
90
4
8
12
16
time (yrs)
300 md
confined
300 md:
unconfined
3000 md:
confined
3000 md: unconfined
ambient
confined
unconfined
distance profiles
at max pressure
300 md
confined
300 md unconf.
3000 md:
confined
200
400
600
800
distance from injection (m)

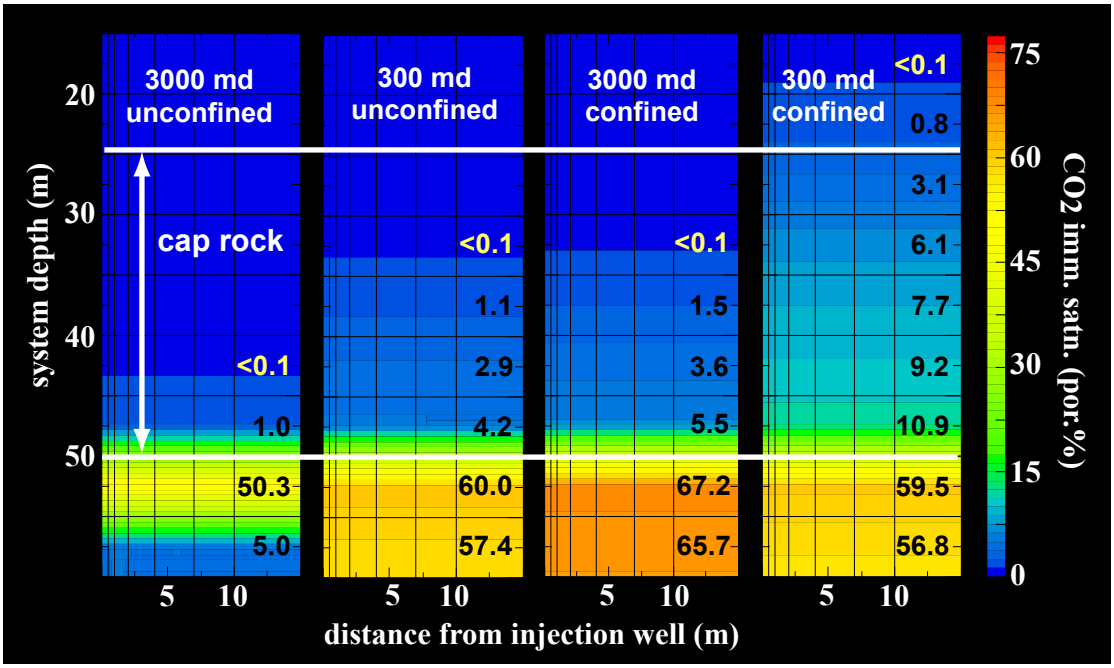
3000 md
unconfined
300 md
unconfined
3000 md
confined
300 md
confined
cap rock
<0.1
1.0
50.3
5.0
<0.1
1.1
2.9
4.2
60.0
57.4
<0.1
1.5
3.6
5.5
67.2
65.7
<0.1
0.8
3.1
6.1
7.7
9.2
10.9
59.5
56.8
20
30
40
50
system depth (m)
5
10
distance from injection well (m)
75
60
45
30
15
0
CO2 imm. satn. (por.%)

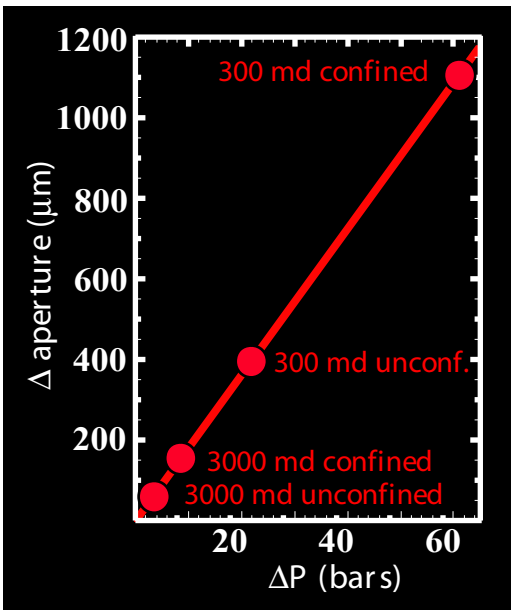
1200
1000
800
600
400
200
Δ aperture (μm)
300 md confined
300 md unconf.
3000 md confined
3000 md unconfined
20
40
60
ΔP (bars)

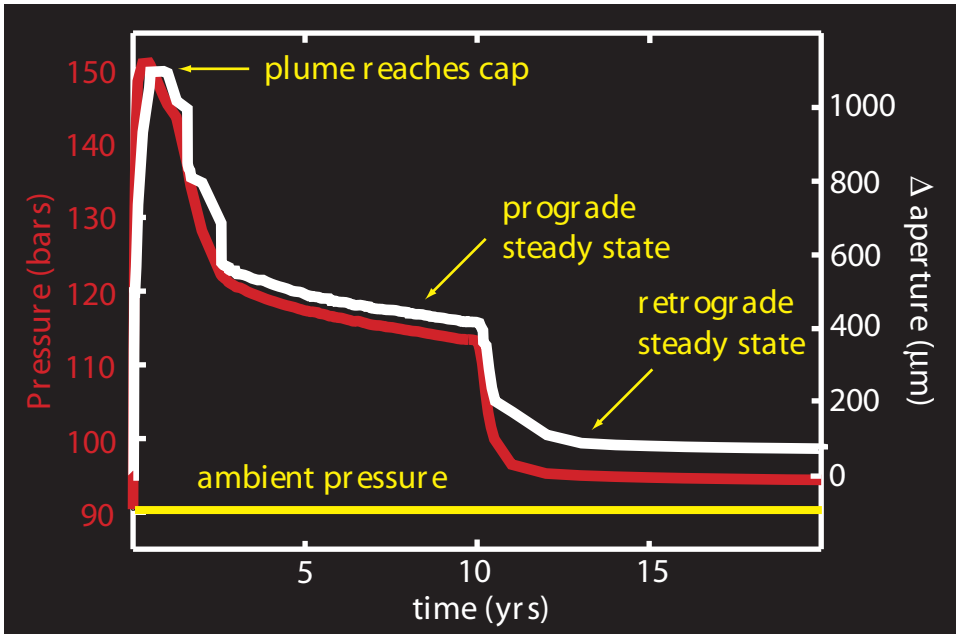
plume reaches cap
prograde
steady state
retrograde
steady state
ambient pressure
Pressure (bars)
150
140
130
120
110
100
90
Δ aperture (μm)
1000
800
600
400
200
0
5
10
15
time (yrs)

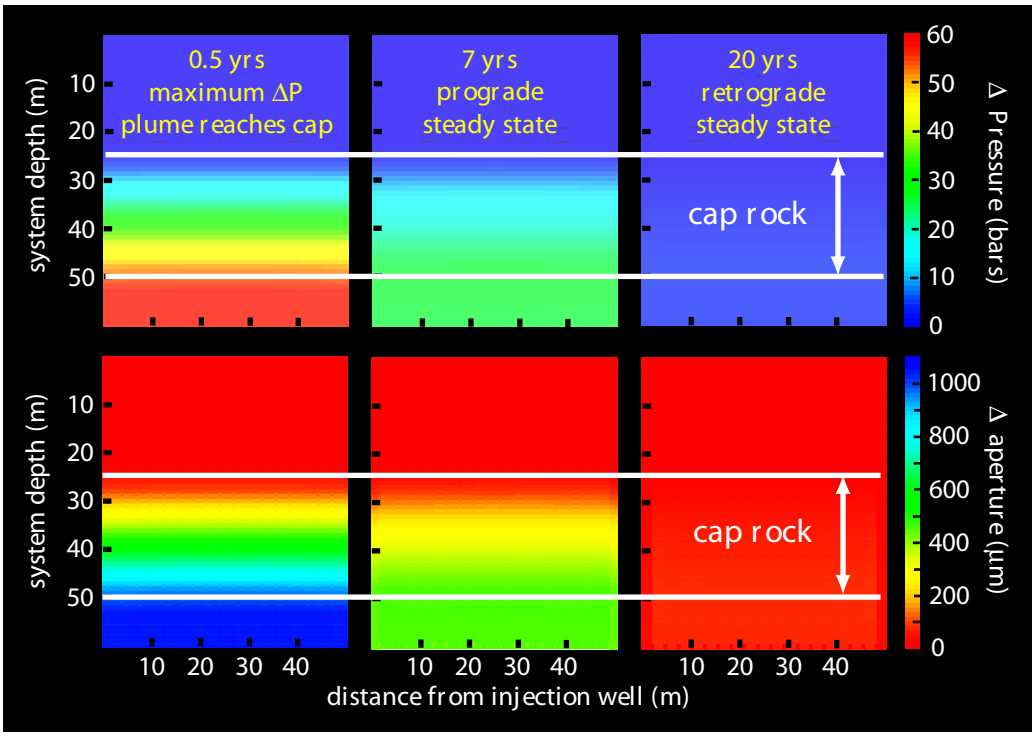
0.5 yrs
maximum ΔP
plume reaches cap
7 yrs
prograde
steady state
20 yrs
retrograde
steady state
cap rock
cap rock
system depth (m)
system depth (m)
10
20
30
40
50
Δ Pressure (bars)
60
50
40
30
20
10
0
Δ aperture (μm)
1000
800
600
400
200
0
10 20 30 40
10 20 30 40
10 20 30 40
distance from injection well (m)

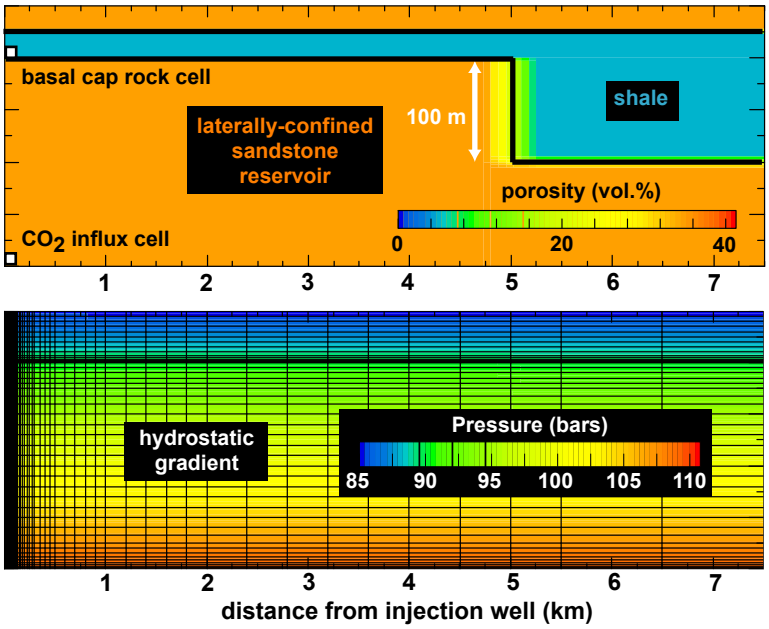
basal cap rock cell
laterally-confined sandstone reservoir
100 m
shale
porosity (vol.%)
0
20
40
CO_2 influx cell
1
2
3
4
5
6
7
hydrostatic gradient
Pressure (bars)
85
90
95
100
105
110
1
2
3
4
5
6
7
distance from injection well (km)

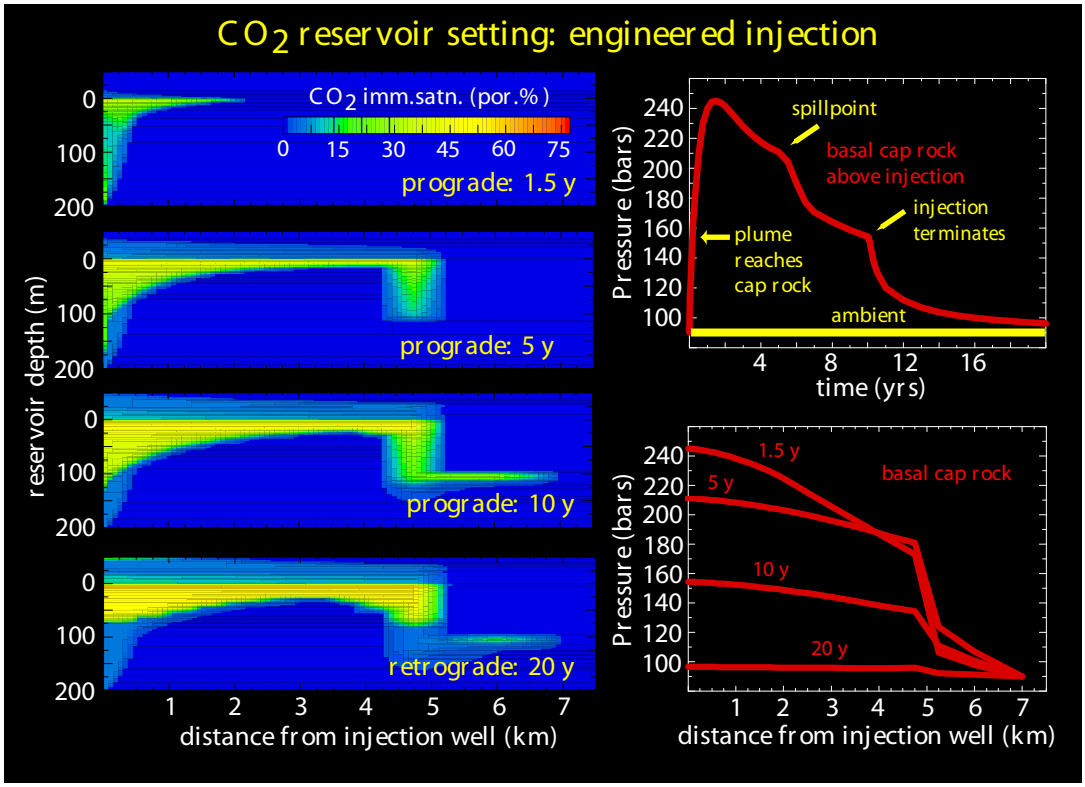
CO2 reservoir setting: engineered injection
CO2 imm.satn. (por.%)
0 15 30 45 60 75
prograde: 1.5 y
prograde: 5 y
prograde: 10 y
retrograde: 20 y
reservoir depth (m)
0
100
200
1 2 3 4 5 6 7
distance from injection well (km)
Pressure (bars)
240 220 200 180 160 140 120 100
spillpoint
basal cap rock above injection
injection terminates
plume reaches cap rock
ambient
4 8 12 16
time (yrs)
1.5 y
5 y
10 y
20 y
basal cap rock
distance from injection well (km)

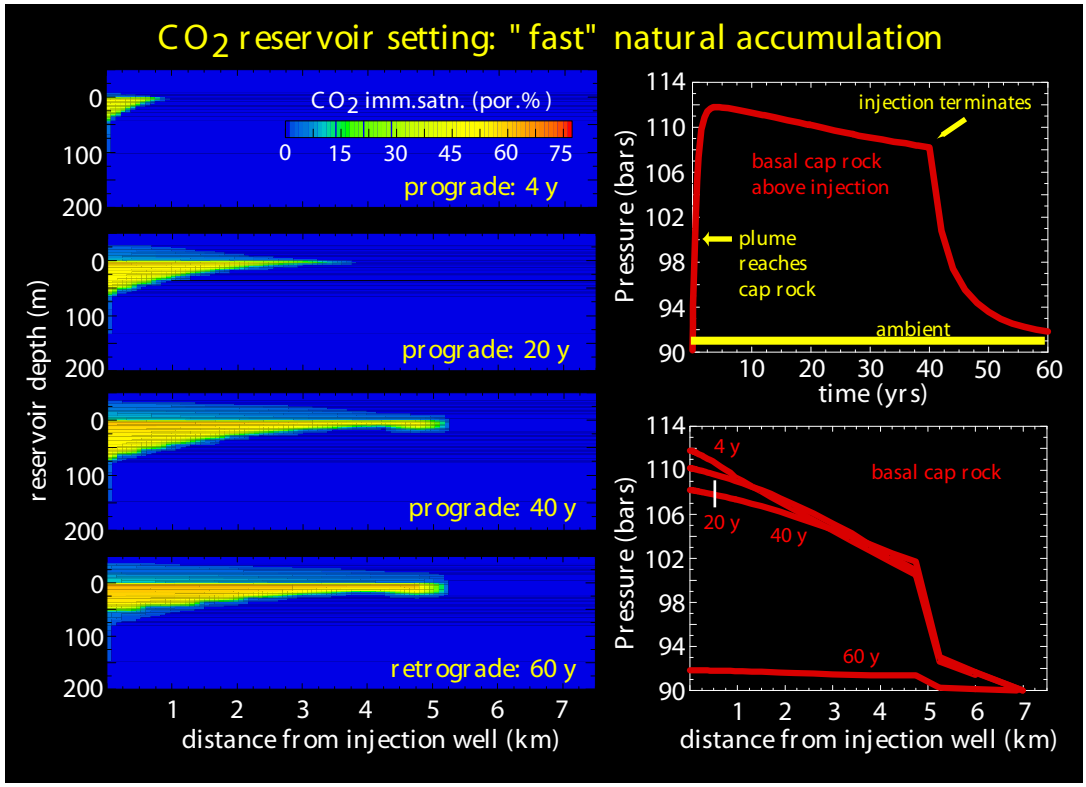
CO2 reservoir setting: "fast" natural accumulation
CO2 imm.satn. (por.%)
0 15 30 45 60 75
prograde: 4 y
prograde: 20 y
prograde: 40 y
retrograde: 60 y
reservoir depth (m)
0
100
200
distance from injection well (km)
1 2 3 4 5 6 7
Pressure (bars)
114
110
106
102
98
94
90
injection terminates
basal cap rock
above injection
plume
reaches
cap rock
ambient
time (yrs)
10 20 30 40 50 60
4 y
20 y
40 y
60 y
basal cap rock

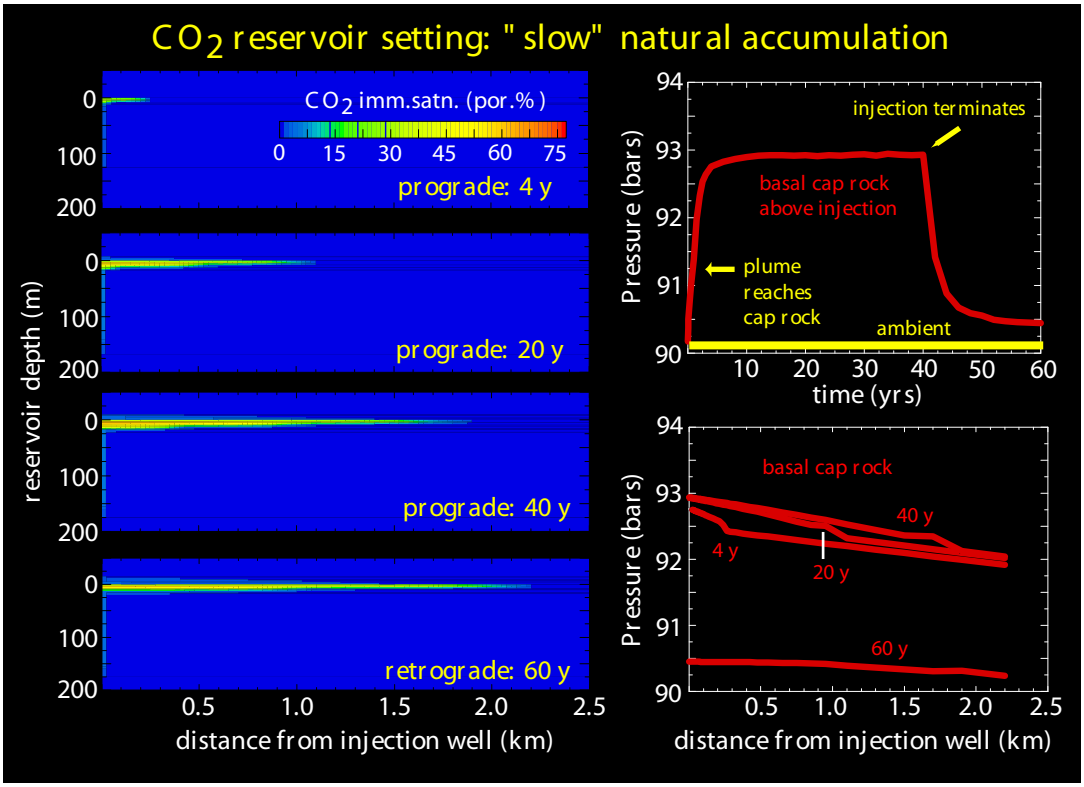
CO2 reservoir setting: "slow" natural accumulation
CO2 imm.satn. (por.%)
0 15 30 45 60 75
prograde: 4 y
prograde: 20 y
prograde: 40 y
retrograde: 60 y
reservoir depth (m)
0
100
200
0.5 1.0 1.5 2.0 2.5
distance from injection well (km)
injection terminates
basal cap rock above injection
plume reaches cap rock
ambient
Pressure (bars)
94
93
92
91
90
10 20 30 40 50 60
time (yrs)
basal cap rock
40 y
4 y
20 y
60 y
Pressure (bars)
distance from injection well (km)

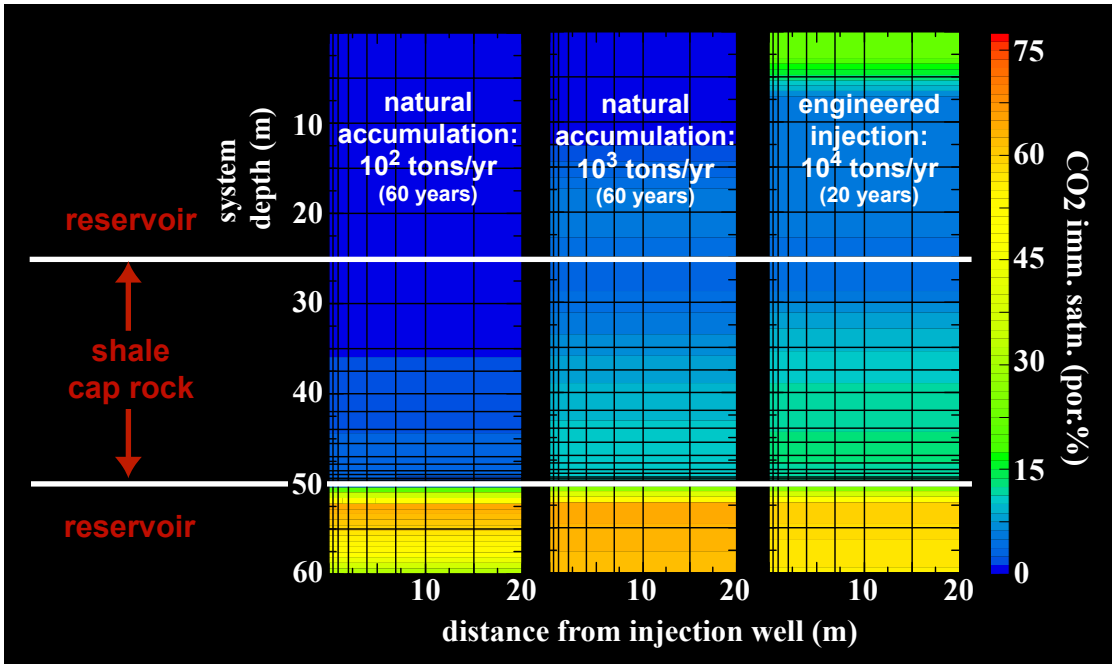
natural accumulation: 10^2 tons/yr (60 years)
natural accumulation: 10^3 tons/yr (60 years)
engineered injection: 10^4 tons/yr (20 years)
reservoir
shale cap rock
reservoir
system depth (m)
10
20
30
40
50
60
10
20
10
20
10
20
distance from injection well (m)
75
60
45
30
15
0
CO2 imm. satn. (por.%)

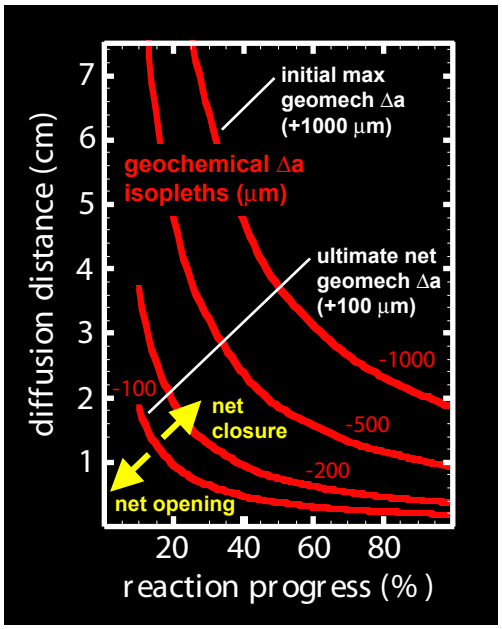
initial max
geomech Δa
(+1000 μm)
geochemical Δa
isopleths (μm)
ultimate net
geomech Δa
(+100 μm)
-1000
-100
net
closure
-500
-200
net opening
diffusion distance (cm)
reaction progress (%)
1
2
3
4
5
6
7
20
40
60
80